A direct numerical simulation study on the mean velocity characteristics in turbulent pipe flow

XIAOHUA WU[1] AND PARVIZ MOIN[2]

[1]Department of Mechanical Engineering, Royal Military College of Canada,
Kingston, Ontario, Canada K7K 7B4
Xiaohua.Wu@rmc.ca

[2]Center for Turbulence Research, Stanford University, Stanford CA 94305–3035, USA
moin@stanford.edu

Fully developed incompressible turbulent pipe flow at bulk-velocity- and pipe-diameter-based Reynolds number $Re_D = 44\,000$ was simulated with second-order finite-difference methods on 630 million grid points. The corresponding Kármán number R^+, based on pipe radius R, is 1142, and the computational domain length is $15R$. The computed mean flow statistics agree well with Princeton Superpipe data at $Re_D = 41\,727$ and at $Re_D = 74\,000$. Second-order turbulence statistics show good agreement with experimental data at $Re_D = 38\,000$. Near the wall the gradient of $\ln \overline{u}_z^+$ with respect to $\ln(1-r)^+$ varies with radius except for a narrow region, $70 < (1-r)^+ < 120$, within which the gradient is approximately 0.149. The gradient of $\overline{u}_z^+$ with respect to $\ln\{(1-r)^+ + a^+\}$ at the present relatively low Reynolds number of $Re_D = 44\,000$ is not consistent with the proposition that the mean axial velocity $\overline{u}_z^+$ is logarithmic with respect to the sum of the wall distance $(1-r)^+$ and an additive constant a^+ within a mesolayer below 300 wall units. For the standard case of $a^+ = 0$ within the narrow region from $(1-r)^+ = 50$ to 90, the gradient of $\overline{u}_z^+$ with respect to $\ln\{(1-r)^+ + a^+\}$ is approximately 2.35. Computational results at the lower Reynolds number $Re_D = 5300$ also agree well with existing data. The gradient of $\overline{u}_z$ with respect to $1-r$ at $Re_D = 44\,000$ is approximately equal to that at $Re_D = 5300$ for the region of $1-r > 0.4$. For $5300 < Re_D < 44\,000$, bulk-velocity-normalized mean velocity defect profiles from the present DNS and from previous experiments collapse within the same radial range of $1-r > 0.4$. A rationale based on the curvature of mean velocity gradient profile is proposed to understand the perplexing existence of logarithmic mean velocity profile in very-low-Reynolds-number pipe flows. Beyond $Re_D = 44\,000$, axial turbulence intensity varies linearly with radius within the range of $0.15 < 1-r < 0.7$. Flow visualizations and two-point correlations reveal large-scale structures with comparable near-wall azimuthal dimensions at $Re_D = 44\,000$ and 5300 when measured in wall units. When normalized in outer units, streamwise coherence and azimuthal dimension of the large-scale structures in the pipe core away from the wall are also comparable at these two Reynolds numbers.

1. Introduction

Fully developed incompressible turbulent flow through a smooth pipe is a canonical problem in fluid mechanics. Celebrated experimental data sets by Nikuradse and Laufer on mean and turbulence statistics for the pipe flow appeared more than a

half-century ago, along with the classical complete similarity theory by Millikan on logarithmic mean velocity distribution with universal coefficients for the intermediate inertial sublayer. Those early studies were summarized in, for example, Hinze (1975). Recently, the issue of mean pipe velocity profile has been revisited in a number of experimental and theoretical investigations. Noticeably absent from the recent examinations of the mean pipe flow velocity profile is direct numerical simulation (DNS), which has played a vital role in the advancement of wall turbulence research over the past two decades. To this end there is a need for new pipe flow DNS data at Reynolds numbers substantially higher than those achieved previously. In the absence of relevant and accurate DNS pipe flow data previous authors frequently invoked the low-Reynolds-number DNS channel flow results in their studies on mean pipe flow theory. This paper describes our pipe flow DNS statistics at $Re_D = 44\,000$ acquired from a large-scale parallel computation. Simulation at a lower Reynolds number of $Re_D = 5300$ is also presented.

Previous representative DNS pipe flow work can be found in Eggels *et al.* (1994). The Reynolds number used in Eggels *et al.* is $Re_D = 5300$. Axial dimension of their computational domain was $10R$. Their computation was performed on a finite-volume mesh of $96 \times 128 \times 256$ along the r, θ, z directions, respectively. Orlandi & Fatica (1997) and Fukagata & Kasagi (2002) simulated the same pipe flow as that of Eggels *et al.* with a second-order finite-difference method. The turbulent pipe flow at $Re_D = 5600$ was computed by Loulou *et al.* (1997) with a hybrid B-spline spectral method on a $72 \times 160 \times 192$ mesh. Wagner, Huttl & Friedrich (2001) and Veenman (2004) simulated the pipe flow at $Re_D = 10\,300$ with a finite-volume method and a pseudo-spectral method, respectively. Flow and heat transfer computation in a turbulent pipe flow was reported by Satake, Kunugi & Himeno (2000) for $Re_D = 40\,000$. Their numerical approach is second-order finite-volume discretization. They used a mesh size of $512 \times 768 \times 1024$ along the r, θ and z directions, respectively. The corresponding grid resolution was $\Delta z^+ = 15.4$ and $\Delta(R\theta)^+ = 8.6$, and the streamwise extent of their computational box was $15R$.

Barenblatt, Chorin & Prostokishin (1997) proposed that, for smooth pipe flow, the widely accepted universal logarithmic law should be replaced by an incomplete similarity power law where the power exponent and multiplicative factor depend on the flow Reynolds number. They showed that the theoretical overlap arguments that led to the logarithmic law also support their power law at least as much as they support the universal logarithmic law. In addition, Barenblatt *et al.* analysed the classical Nikuradse pipe flow data for $Re_D > 4000$ and found that they favour the power law more than the logarithmic law. The coefficients for their proposed power law were obtained by curve-fitting to the Nikuradse data. The suggested applicable region for the power law is approximately from the top of the buffer layer $(1-r)^+ = 40$ to $0.9R$, covering almost the entire pipe flow cross-section. The idea that mean velocity distribution in a turbulent pipe flow can be well approximated by a simple power-type formula with Reynolds number dependent exponent is not new (see the discussion in Hinze 1975). The point of Barenblatt *et al.* (1997) is that this power law representation is more than an empirical coincidence.

Zagarola, Perry & Smits (1997) and Zagarola & Smits (1998) reported mean pipe flow experimental data collected from the Princeton Superpipe facility, spanning a range from $Re_D = 31\,500$ to 35×10^6. Adhering to the classical approach, they focused on the overlap region above the buffer layer but below $1 - r = 0.1R$ or $(1-r)^+ = 0.1R^+$ instead of the much wider range in Barenblatt *et al.* (1997). $R^+ = u_\tau R/\nu$ is often referred to as the Kárman number. Zagarola *et al.* (1997) emphasized the possible

coexistence of a power law and a log law in the mean velocity distribution. Specifically, for relatively low-Reynolds-number flows in which $R^+ < 5000$, there exists a power law within the region of $50 < (1 - r)^+ < 0.1R^+$. For higher-Reynolds-number flows in which $R^+ > 5000$, there is a power law for $50 < (1 - r)^+ < 500$, followed by a log law for $500 < (1 - r)^+ < 0.1R^+$.

Barenblatt & Chorin (1998) found that the Princeton Superpipe data are consistent with the Nikuradse data to the extent of $Re_D < 1.0 \times 10^6$. They commented that the experimental data of Zagarola *et al.* (1997) beyond $Re_D = 1.0 \times 10^6$ are affected by surface roughness. However, Smits & Zagarola (1998) stated that effect of roughness on their data is negligible for $Re_D < 36 \times 10^6$.

Wosnik, Castillo & George (2000) (see also Oberlack 2001) proposed that, inside the overlap region of $30 < (1 - r)^+ < 0.1R^+$, the mean velocity profile is logarithmic with respect to $(1 - r)^+ + a^+$, where a^+ is an offset parameter and is approximately -8 for pipe flow. The role of a^+ was related to a mesolayer existing in the region of $30 < (1 - r)^+ < 300$. Wosnik *et al.* suggested that their mesolayer theory is applicable for R^+ as low as 180. They disputed the extended power law of Barenblatt & Chorin (1998), and they also disagreed with the limited power law of Zagarola *et al.* (1997). Wosnik *et al.* believed that the experimental data of Zagarola *et al.* (1997) are free of surface roughness effects at high-Reynolds-number range, but commented that inside the mesolayer the Princeton Superpipe data may not be accurate. Wosnik *et al.* (2000) attempted to validate their theory by evaluating the velocity gradients but found that the noisy mean velocity gradient profiles calculated from the existing experimental pipe flow data are not helpful in their validation effort.

Perry, Hafez & Chong (2001) emphasized the importance of applying corrections to pipe flow experimental data with respect to the effect of turbulence intensity as well as the effect of probe size. They conjectured that the data of Zagarola *et al.* (1997) and Zagarola & Smits (1998) may be influenced by surface roughness. Based on these corrections, Perry *et al.* (2001) pointed out that the classical mean velocity theory for turbulent pipe flow is still valid and the limited power law from Zagarola *et al.* (1997) may be due to data processing error.

McKeon *et al.* (2004a) and Morrison *et al.* (2004) repeated the Superpipe experiments of Zagarola & Smits (1998) with improved equipment and procedure. Their new experimental data affirmed the limited power law of Zagarola & Smits (1998), but with a narrower applicable range of $50 < (1 - r)^+ < 300$. The log law further away from the wall was also verified and was found to be valid for $600 < (1 - r)^+ < 0.12R^+$. Implicit in their conclusion is that, for low Reynolds number flows in which $0.12R^+ < 600$, there is no log law and only the power law applies. McKeon *et al.* (2004a) also confirmed that the effect from surface roughness in the Princeton Superpipe data is negligible.

Wei *et al.* (2005) analysed the mean momentum balance equation for turbulent pipe flow, among other wall-bounded flows. Instead of comparing the relative magnitude of viscous and shear stresses, they noted that gradients of these stresses are more relevant. Wei *et al.* found that existing data and their theoretical arguments support the notion of two logarithmic regions.

It is difficult for pipe flow DNS, at the present time, to enter directly into the debate on power law versus log law in the inertial sublayer, because one would need to exceed $Re_D = 230\,000$ or $R^+ = 5000$ by a wide margin to have a meaningful inertial sublayer. Our DNS results at $Re_D = 44\,000$ ($R^+ = 1142$) exhibit limited power-type behaviour for $70 < (1 - r)^+ < 120$, and at the same time approximate logarithmic behaviour for $50 < (1 - r)^+ < 90$.

The established logarithmic dependence of $\overline{u}_z^+$ on $(1-r)^+$ in very-low-Reynolds-numbers turbulent flows, $R^+ = 180$ for example, is confusing and has not been well explained in previous studies. In such flows two of the basic assumptions involved in Millikan's arguments are not applicable, namely, universal inner scaling of $\overline{u}_z^+$ on $(1-r)^+$ near the wall and universal outer scaling of $[\overline{u}_z(r=0) - \overline{u}_z]/u_\tau$ on $1-r$ away from the wall (defect law). In this work we argue that the approximate logarithmic variation of $\overline{u}_z^+$ on $(1-r)^+$ is dictated by the nature of the curvature of the mean velocity gradient profile.

2. Details of the present computation

2.1. *Governing equations*

We consider incompressible, fully developed turbulent flow through a smooth pipe with radius R. The governing equations are the continuity and Navier–Stokes equations for incompressible flow in cylindrical coordinates:

$$\frac{1}{r}\frac{\partial r u_r}{\partial r} + \frac{1}{r}\frac{\partial u_\theta}{\partial \theta} + \frac{\partial u_z}{\partial z} = 0, \tag{2.1}$$

$$\frac{\partial u_r}{\partial t} + u_r\frac{\partial u_r}{\partial r} + \frac{u_\theta}{r}\frac{\partial u_r}{\partial \theta} + u_z\frac{\partial u_r}{\partial z} - \frac{u_\theta^2}{r}$$
$$= -\frac{1}{\rho}\frac{\partial p}{\partial r} + \nu\left\{\frac{\partial^2 u_r}{\partial r^2} + \frac{1}{r^2}\frac{\partial^2 u_r}{\partial \theta^2} + \frac{\partial^2 u_r}{\partial z^2} + \frac{1}{r}\frac{\partial u_r}{\partial r} - \frac{2}{r^2}\frac{\partial u_\theta}{\partial \theta} - \frac{u_r}{r^2}\right\}, \tag{2.2}$$

$$\frac{\partial u_\theta}{\partial t} + u_r\frac{\partial u_\theta}{\partial r} + \frac{u_\theta}{r}\frac{\partial u_\theta}{\partial \theta} + u_z\frac{\partial u_\theta}{\partial z} + \frac{u_r u_\theta}{r}$$
$$= -\frac{1}{\rho r}\frac{\partial p}{\partial \theta} + \nu\left\{\frac{\partial^2 u_\theta}{\partial r^2} + \frac{1}{r^2}\frac{\partial^2 u_\theta}{\partial \theta^2} + \frac{\partial^2 u_\theta}{\partial z^2} + \frac{1}{r}\frac{\partial u_\theta}{\partial r} + \frac{2}{r^2}\frac{\partial u_r}{\partial \theta} - \frac{u_\theta}{r^2}\right\}, \tag{2.3}$$

$$\frac{\partial u_z}{\partial t} + u_r\frac{\partial u_z}{\partial r} + \frac{u_\theta}{r}\frac{\partial u_z}{\partial \theta} + u_z\frac{\partial u_z}{\partial z}$$
$$= -\frac{1}{\rho}\frac{\partial p}{\partial z} + \nu\left\{\frac{\partial^2 u_z}{\partial r^2} + \frac{1}{r^2}\frac{\partial^2 u_z}{\partial \theta^2} + \frac{\partial^2 u_z}{\partial z^2} + \frac{1}{r}\frac{\partial u_z}{\partial r}\right\}. \tag{2.4}$$

In the present study, the unit length scale is pipe radius R, and the unit velocity scale is $\overline{u}_{bulk}$, which is defined as the ratio of mean mass flow rate and pipe cross-sectional area. The unit time scale is therefore $R/\overline{u}_{bulk}$. The imposed streamwise pressure gradient $\partial \overline{p}/\partial z$ is adjusted during the simulation to maintain constant mass flow rate, i.e. $\overline{u}_{bulk} = 1.0$. An overbar denotes ensemble averaging, superscript $+$ refers to normalized quantities by friction velocity u_τ for velocity, and by viscous wall unit ν/u_τ for distance; r is the radial coordinate measured from pipe axis, z is the flow axial direction, and θ is the azimuthal coordinate. Since the unit length scale is pipe radius R, $1-r$ represents distance from the wall.

2.2. *Numerical method*

The computer program solves the governing equations (2.1)–(2.4) for instantaneous velocity components (u_r, u_θ, u_z) and pressure p as functions of (r, θ, z, t) in a cylindrical coordinate system with second-order finite-difference method. In the computational mesh velocity components are staggered with respect to pressure; refer to figure 4.5 of Pierce & Moin (2001). Conservation of kinetic energy in the inviscid limit by the numerical scheme is facilitated by the use of staggering. In the immediate vicinity of pipe axis all quantities except for u_r are staggered in the

radial direction with respect to the centreline, i.e. they are located at $\Delta r/2$ from the centreline, and u_r is collocated with the centreline. Centreline conditions are therefore not required for any of the variables except for u_r. Centreline condition for u_r is obtained by averaging corresponding values across the centreline (Pierce & Moin 2001). Derivatives of quantities that are staggered with respect to the centreline can be obtained by differencing opposing values across the centreline, accounting for reversals in the directions of radial unit vector through the centreline. No-slip conditions were used for velocities at the wall. Periodic boundary conditions are applied in the streamwise and azimuthal directions for the fully developed turbulent pipe flow. The time advancement method used to solve the time-dependent, three-dimensional constant density Navier–Stokes equations is the second-order fractional step method (Kim & Moin 1985). Convection and diffusion terms that involve derivatives in the radial direction or azimuthal direction are treated implicitly. A third-order Runge–Kutta scheme is used for terms treated explicitly and a second-order Crank–Nicolson scheme is used for terms treated implicitly. Poisson equation for pressure is solved by Fast Fourier Transform along the homogeneous directions. Details of the algorithm were described in full in Akselvoll & Moin (1996a) and Pierce & Moin (2001, 2004).

2.3. *Computational details at* $Re_D = 5300$

The experimental study of Kim & Adrian (1999) suggested the existence of very large-scale motions in the form of long regions of outer-layer streamwise fluctuations. The maximum wavelength of the large-scale motion was found to be $12R$ to $14R$. More recent work by the same group reported in Guala, Hommema & Adrian (2006) modified the maximum wavelength to a range from $8R$ to $16R$. Morrison *et al.* (2004) indicated that the maximum wavelength in their pipe flow is approximately $10R$. In view of these findings, a value of $15R$ was chosen for computational domain length in the present numerical study at both Reynolds numbers. This computational domain is 50% longer than that used by Eggels *et al.* (1994).

The finite-difference grid size used in the present simulation at $Re_D = 5300$ is $256 \times 512 \times 512$ along the r, θ and z directions, respectively. The resolution along the axial direction is $\Delta z^+ = 5.31$ or $\Delta z = 0.0293$. Along the azimuthal direction the maximum grid spacing is attained at the wall ($r = R$) with $\Delta(R\theta)^+ = 2.22$ or $\Delta(R\theta) = 0.0123$. The minimum and maximum wall-normal grid spacings are 9.203×10^{-4} and 9.083×10^{-3}, respectively. In wall units, these correspond to 0.167 and 1.647. The maximum wall-normal grid spacing is located at $r = 0.409$. At the pipe centreline the wall-normal grid spacing is 1.845×10^{-3}. The computer program was made parallel using the Message Passing Interface (MPI) library. The simulation was performed using 128 processors on 16 IBM 8-way P655+ nodes. The initial velocity field was random. In the first 700 iterations, the maximum axial CFL component was fixed at a small value of 0.05 and the corresponding time step Δt was approximately 0.0009. This was to allow the start-up effect associated with the imposed unrealistic initial velocity field to diminish. After the first 700 iterations, the computational time step was fixed at $\Delta t = 0.015$ and the maximum allowed axial CFL component was set at 1.0. The actual computed axial CFL component fluctuates around 0.78. The radial and azimuthal CFL components can be rather large because these two directions are treated implicitly; see also Akselvoll & Moin (1996b). Statistics were collected for $20\,000 \Delta t$ beginning from $19\,700 \Delta t$. The sampling time duration is equivalent to $300R/\overline{u}_{bulk}$, enough to allow a particle to travel 20 times through the pipe axial dimension at the bulk velocity. Total simulation time duration for $Re_D = 5300$ was

$585R/\overline{u}_{bulk}$. In addition to averaging in time, the statistical sample was enhanced by averaging in the two homogeneous directions (z, θ).

2.4. Computational details at $Re_D = 44\,000$

The finite-difference grid size used in the current computation at $Re_D = 44\,000$ is $300 \times 1024 \times 2048$ along the r, θ and z directions, respectively. The total number of grid points is 200 times larger than that used by Eggels *et al.* (1994). Resolution along the axial direction is $\Delta z^+ = 8.37$ or $\Delta z = 0.00732$. Along the azimuthal direction maximum grid spacing is achieved at the wall $(r = R)$ yielding $\Delta(R\theta)^+ = 7.01$ or $\Delta(R\theta) = 0.00614$. The minimum and maximum wall-normal grid spacings are 3.578×10^{-4} and 9.892×10^{-3}, respectively. In wall units, these correspond to 0.41 and 11.3. The maximum wall-normal grid spacing is located at $r = 0.406$ rather than at the centreline. The first layer of grid points in the staggered mesh system is located at 0.205 wall units away from the pipe surface. There are 108 grid points located near the wall between $0 < (1 - r) < 0.1$, and 44 grid points near the centreline between $0.9 < (1 - r) < 1.0$. At the pipe centreline the wall-normal grid spacing is 1.435×10^{-3}.

The simulation was performed using 1024 processors on 128 IBM 8-way P655+ nodes. Each restart data file has a size of 25GB. Initial conditions are the same as those used in the $Re_D = 5300$ computation. During the first 400 iterations, the maximum axial CFL component was fixed at a small value of 0.05 and the corresponding time step Δt was approximately 0.0002. This is again to accommodate start-up effects associated with the imposed unrealistic initial velocity field. After the first 400 iterations, the computational time step was fixed at $\Delta t = 0.005$ and the maximum allowed axial CFL component was set to be 1.25. The actual computed axial CFL component fluctuates during the simulation around 1.0. Statistics were collected for $30\,000\Delta t$ starting from $20\,400\Delta t$. The sampling time duration is equivalent to $150R/\overline{u}_{bulk}$, enough to allow a particle to travel 10 times through the pipe axial dimension at the bulk velocity. Total computed time duration was $250R/\overline{u}_{bulk}$.

3. Statistics at $Re_D = 5300$

Reliability of the current parallel computer code may be demonstrated partially through comparison with existing pipe flow DNS results at low Reynolds numbers. Previously, Toonder & Nieuwstadt (1997) compared their LDV experimental data at $Re_D = 4900$ with the DNS of Eggels *et al.* (1994) at $Re_D = 5300$. Their figures indicate that, among their presented quantities, the two sets of results agree quite well. Figures 1 to 5 present a comparison of the present mean and second-order statistics with the results from Eggels *et al.* at $Re_D = 5300$ and with those from Loulou *et al.* at a slightly higher Reynolds number of $Re_D = 5600$. The present friction velocity u_τ is $0.06844\overline{u}_{bulk}$, compared to $0.06789\overline{u}_{bulk}$ in Eggels *et al.* From figure 1 it is easy to see that the grid resolution used by Eggels *et al.* in the near-wall region is coarser than in the present simulation. The first two grid points in their calculation were located at $(1 - r)^+ \approx 1$ and 2.8, respectively. Turbulence intensities from the present DNS and that of Eggels *et al.* agree well, especially considering the differences in the computational domain size and grid resolution. The largest discrepancy is found in the peak value of azimuthal turbulence intensity $u'^+_{\theta,\text{r.m.s.}}$. Toonder & Nieuwstadt (1997) did not present comparison with Eggels *et al.* on the quantity of $u'^+_{\theta,\text{r.m.s.}}$. Figure 5 shows that the agreement between the current turbulent shear stress $\overline{u'_z u'_r}^+$ with that of Eggels *et al.*
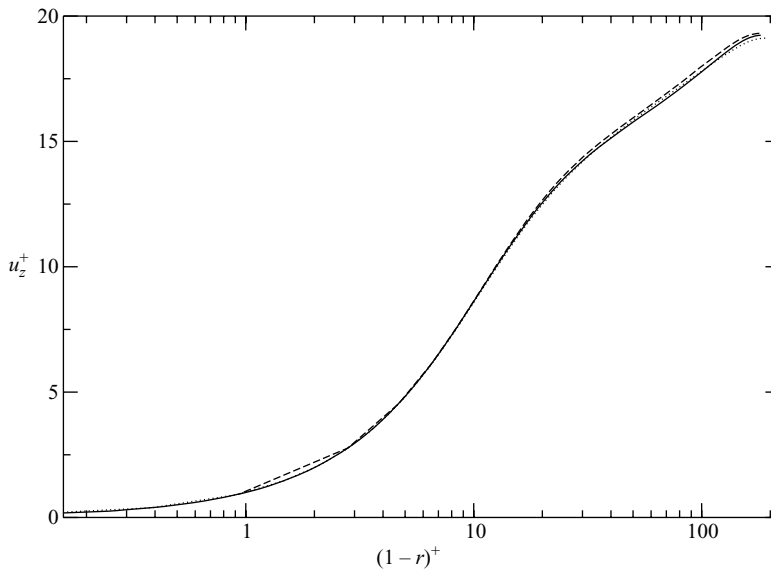
FIGURE 1. Mean axial velocity $\overline{u}_z^+$ as a function of $(1-r)^+$. Solid line: present DNS at $Re_D = 5300$; dashed line: Eggels *et al.* (1994) at $Re_D = 5300$; dotted line: Loulou *et al.* (1997) at $Re_D = 5600$.
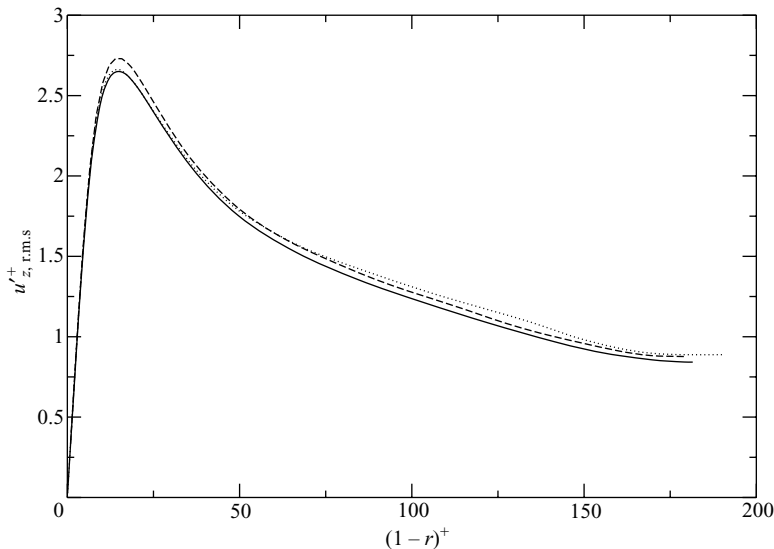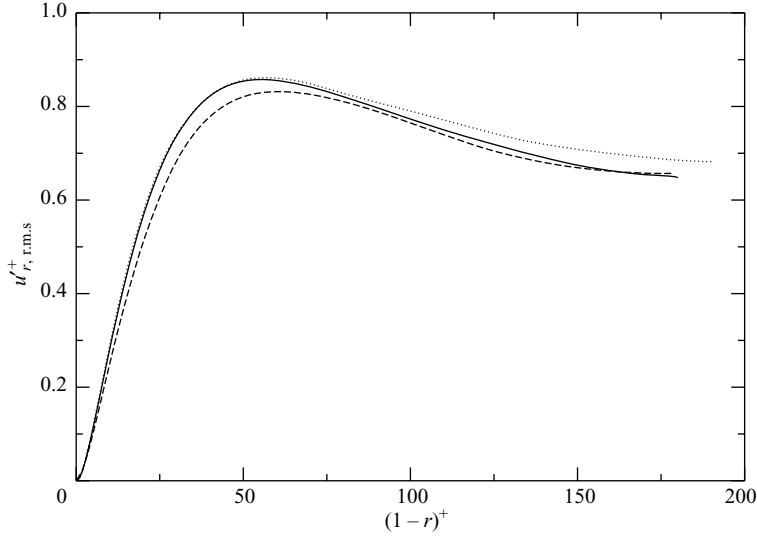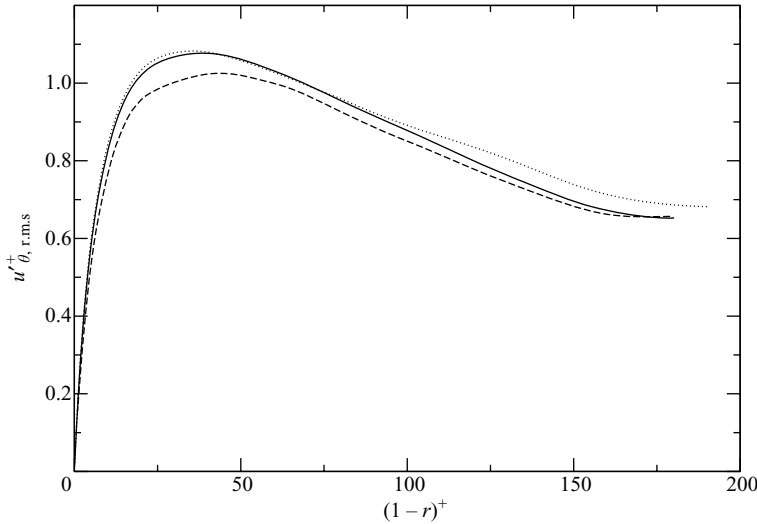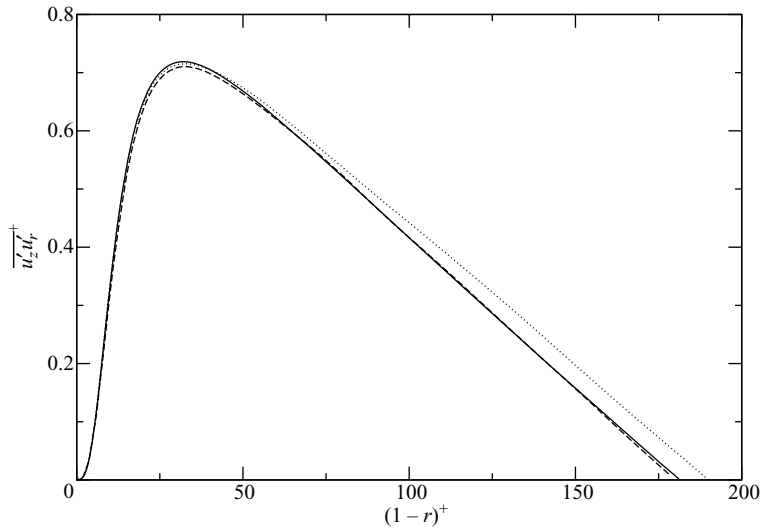

FIGURE 2. Axial turbulence intensity $u'^+_{z,\text{r.m.s.}}$ as a function of $(1-r)^+$. Solid line: present DNS at $Re_D = 5300$; dashed line: Eggels *et al.* (1994) at $Re_D = 5300$; dotted line: Loulou *et al.* (1997) at $Re_D = 5600$.

(1994) is excellent. The small discrepancies in turbulence intensities between the two simulations at $Re_D = 5300$ are all consistent with the expected dependencies of these quantities on the grid resolution. In coarse DNS or LES calculations the streamwise component of turbulence intensity is amplified, whereas the other components are

FIGURE 3. Wall-normal turbulence intensity $u'^{+}_{r,\text{r.m.s.}}$ as a function of $(1-r)^{+}$. Solid line: present DNS at $Re_D = 5300$; dashed line: Eggels *et al.* (1994) at $Re_D = 5300$; dotted line: Loulou *et al.* (1997) at $Re_D = 5600$.

FIGURE 4. Azimuthal turbulence intensity $u'^{+}_{\theta,\text{r.m.s.}}$ as a function of $(1-r)^{+}$. Solid line: present DNS at $Re_D = 5300$; dashed line: Eggels *et al.* (1994) at $Re_D = 5300$; dotted line: Loulou *et al.* (1997) at $Re_D = 5600$.

lower than those in resolved calculations. The present simulation has finer resolution than in Eggels *et al.* and has lower $u'^{+}_{z,\text{r.m.s.}}$ and higher $u'^{+}_{\theta,\text{r.m.s.}}$ and $u'^{+}_{r,\text{r.m.s.}}$ as well as $\overline{u'_z u'_r}^{+}$. The turbulence intensities from Loulou *et al.* (1997) at $R^{+} = 190$ agree very well with the present results at $R^{+} = 180$ in the near-wall region, but are slightly higher in the pipe core, possibly due to the larger Reynolds number used in their simulation.

FIGURE 5. Turbulent shear stress $\overline{u_z'u_r'}^+$ as a function of $(1-r)^+$. Solid line: present DNS at $Re_D = 5300$; dashed line: Eggels *et al.* (1994) at $Re_D = 5300$; dotted line: Loulou *et al.* (1997) at $Re_D = 5600$.

4. Statistics at $Re_D = 44\,000$

4.1. *Simulation error and validation*

Note that in this study the unit length is radius $R = 1$ and the unit velocity is $\overline{u}_{bulk} = 1$. Unless otherwise stated, all the results are therefore automatically normalized by proper combinations of R and $\overline{u}_{bulk}$.

The parallel code has been verified through comparison with previous DNS at $Re_D = 5300$. Assessment of the quality of the simulation statistics at $Re_D = 44\,000$ is made by considering the degree to which the spatial- and time-averaged DNS statistics satisfy the mean momentum transport equations. Reynolds-averaged mean transport equations for the fully developed incompressible turbulent pipe flow are

$$-\frac{1}{\rho}\frac{\partial \overline{p}}{\partial x} + \frac{\nu}{r}\frac{d\overline{u}_z}{dr} + \nu\frac{d^2\overline{u}_z}{dr^2} - \frac{\overline{u_z'u_r'}}{r} - \frac{d\overline{u_z'u_r'}}{dr} = 0, \qquad (4.1)$$

and

$$-\frac{1}{\rho}\frac{\partial \overline{p}}{\partial r} - \frac{\overline{u_r'^2} - \overline{u_\theta'^2}}{r} - \frac{d\overline{u_r'^2}}{dr} = 0, \qquad (4.2)$$

respectively, see Hinze (1975). At each radial station r the residuals of equations (4.1) and (4.2) are computed using the present DNS statistics. If there were no numerical error in the solution of the three-dimensional, time-dependent Navier–Stokes equations and if the statistical sample size is sufficiently large, the summed deviation from zero should vanish. From figure 6 it can be seen that the residual of the mean axial momentum equation is less than $8 \times 10^{-5}\overline{u}_{bulk}^2/R$ where the larger values are mostly located near the pipe wall. Relatively large deviation value is also seen right at the pipe axis, which arises due to the imposed centreline boundary condition. The deviation values shown in the figures are not the raw percentage errors in the computed velocity statistics. Rather, they reflect errors in the derived radial gradients of mean velocity, turbulent shear stress and viscous shear stress.
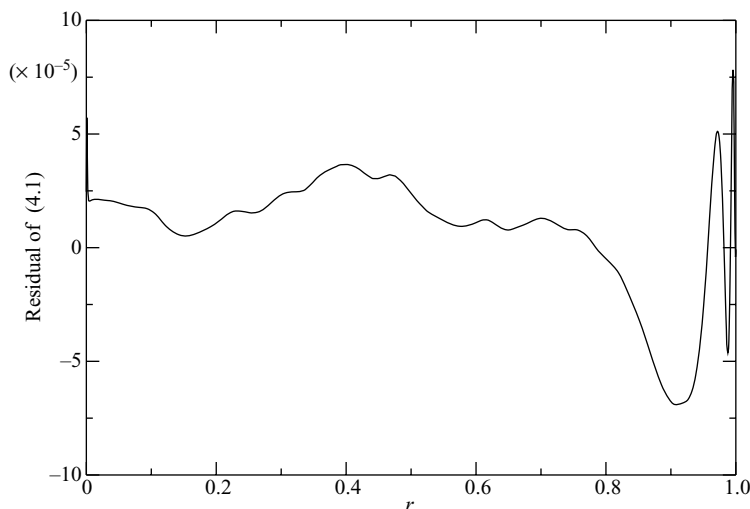
FIGURE 6. Deviation of the DNS statistics at $Re_D = 44\,000$ from the Reynolds-averaged mean axial momentum transport equation (4.1) as a function of r. Normalization is with respect to $\bar{u}_{bulk}^2/R$.

The maximum residual associated with (4.2) was found to be 0.0013 attained in the immediate vicinity of the pipe axis, but away from the axis the error is generally less than 1.0×10^{-5}. Simulation quality at $Re_D = 44\,000$ is further assessed by checking the degree that the present DNS statistics satisfy the integrated mean axial momentum equation,

$$\left(-\nu\frac{\mathrm{d}\bar{u}_z}{\mathrm{d}r} + \overline{u'_z u'_r}\right)^+ - \frac{r}{R} = 0 \qquad (4.3)$$

(see Hinze 1975). The results are shown in figure 7 with a maximum absolute error of less than 0.0025. This error is actually the deviation of the total shear-stress distribution from the theoretical linear profile presented in figure 22. Also shown in the figure is the percentage error of the computed total shear stress relative to the local theoretical value. The maximum error relative to local theoretical value is less than 2%.

The computed wall shear stress τ_w is 2.695×10^{-3}, which gives a Kármán number of $R^+ = 1142$. The corresponding friction factor $f = 8u_\tau^2/\bar{u}_{bulk}^2$ is 0.02156. The present friction factor results at $Re_D = 44\,000$ and 5300 are plotted in figure 8 together with the experimental data of McKeon *et al.* (2004*b*), Durst, Jovanovic & Sender (1995), Toonder & Nieuwstadt (1997) and the DNS data of Loulou *et al.* (1997) in the low-Reynolds-number range of $Re_D < 80\,000$.

The computed mean velocity profile at $Re_D = 44\,000$ also agrees well with the two sets of Princeton Superpipe data: at $Re_D = 41\,727$ (uncorrected) from Zagarola & Smits (1998) and at $Re_D = 74\,000$ from McKeon *et al.* (2004*a*). See figure 9 in wall units and figure 10 in the outer units. The original $\bar{u}_z^+$ data of Zagarola & Smits (1998) for $(1-r)^+ < 30$ are obviously too high but are included here for completeness. Convergence history of the mean axial velocity statistics with increasing sample size is also included in figure 10. Additional convergence history results can be found in figure 21. As expected, both the present DNS and the data of Zagarola & Smits show that in the central region of $0.9 < (1-r) < 1.0$, $\bar{u}_z$ has small variation with radial
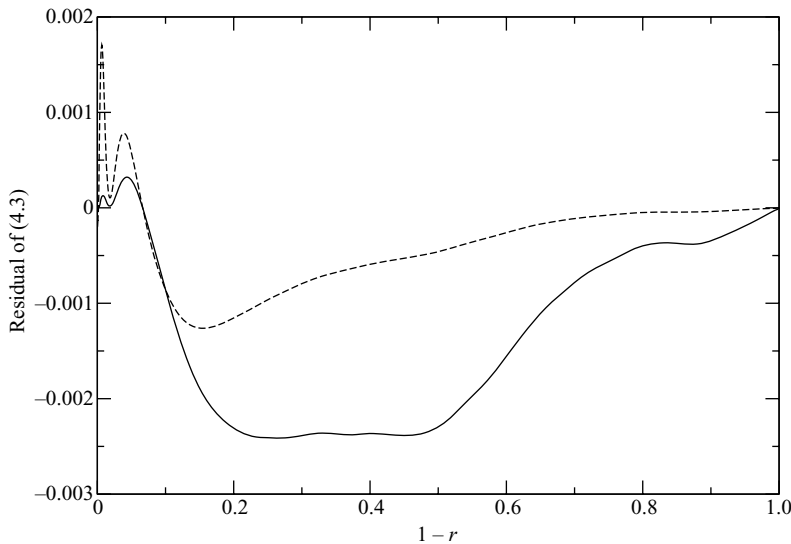
FIGURE 7. Deviation of the DNS statistics at $Re_D = 44\,000$ from the integrated mean axial momentum transport equation (4.3) as a function of $(1 - r)$. Solid line: left-hand side of equation (4.3); dashed line: left-hand side of equation (4.3) divided by $10r/R$.
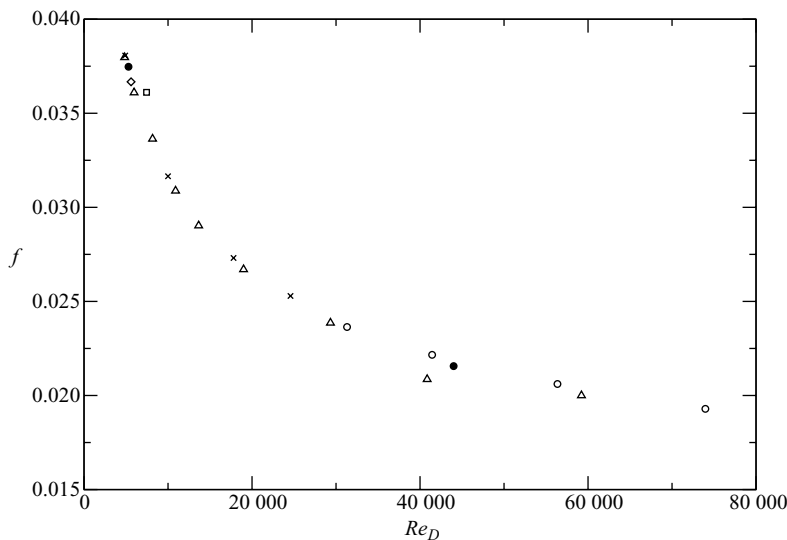

FIGURE 8. Friction factor f as a function of Reynolds number. Solid circle: present DNS; open circle: Princeton data of McKeon *et al.* (2004*b*); diamond: Loulou *et al.* (1997); square: Durst *et al.* (1995); triangle: Oregon data of McKeon *et al.* (2004*b*); cross: Toonder & Nieuwstadt (1997).

distance; there are no data points from McKeon *et al.* in this region. Normalized mean velocity defect $[\overline{u}_z(r=0) - \overline{u}_z]/u_\tau$ is presented in figure 11. Since the defect profiles at different Reynolds numbers do not collapse, it can be concluded that universal velocity defect law does not hold in the range of $5300 < Re_D < 44\,000$. Zagarola & Smits (1998) also noted the poor collapse of $[\overline{u}_z(r=0) - \overline{u}_z]/u_\tau$ profiles at different Reynolds numbers, especially for the region of $(1 - r) < 0.3R$. The absence
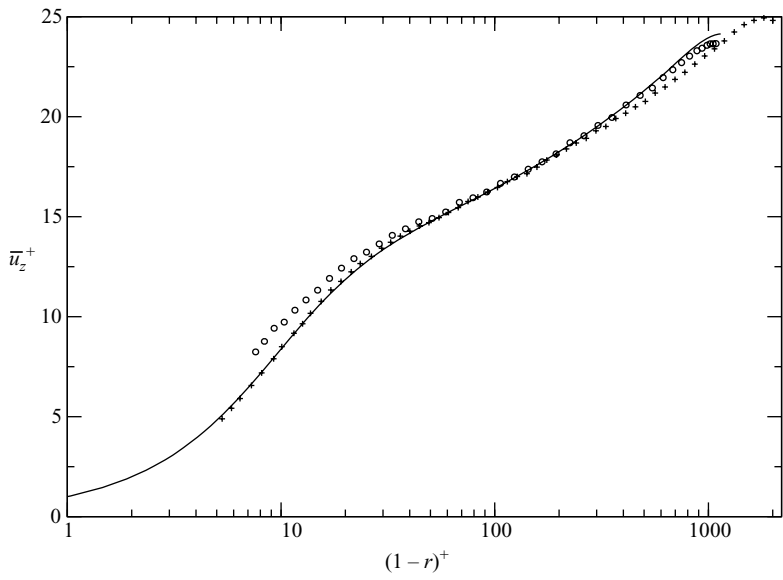
FIGURE 9. Mean velocity $\overline{u}_z^+$ as a function of $(1-r)^+$. Solid line: present DNS at $Re_D = 44\,000$; $+$: McKeon *et al.* (2004*a*) at $Re_D = 74\,000$; circle: Zagarola & Smits (1998) at $Re_D = 41\,727$.
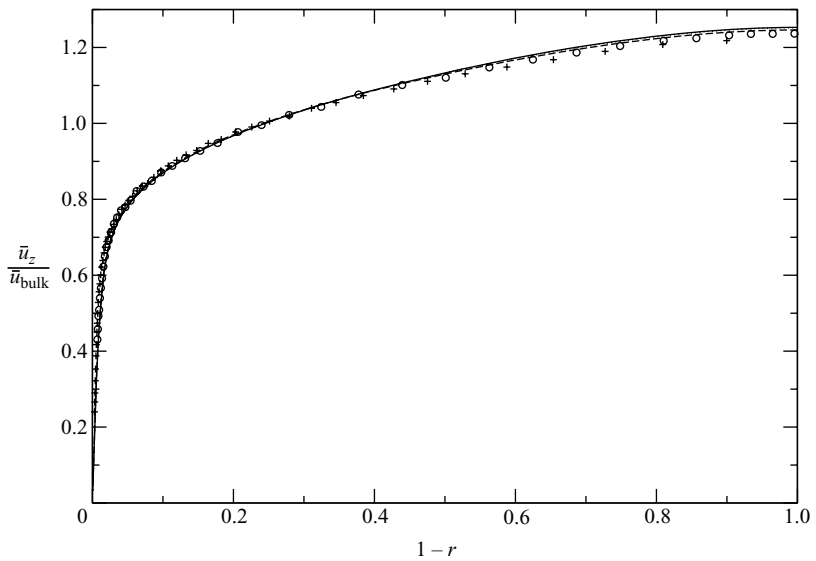

FIGURE 10. Mean velocity $\overline{u}_z/\overline{u}_{bulk}$ as a function of $(1-r)$. Solid line: present DNS at $Re_D = 44\,000$, sampled from $20\,000\Delta t$ to $50\,000\Delta t$; dotted line: sampled from $20\,000\Delta t$ to $40\,000\Delta t$; dashed line: sampled from $20\,000\Delta t$ to $30\,000\Delta t$; $+$: McKeon *et al.* (2004*a*) at $Re_D = 74\,000$; circle: Zagarola & Smits (1998) at $Re_D = 41\,727$.

of universal velocity defect law in turn invalidates the direct application of Millikan's derivation of log law to pipe flows with $Re_D < 44\,000$.

4.2. Mean velocity gradient

Gradient of the mean axial velocity with respect to radial coordinate is shown in figure 12 for $Re_D = 44\,000$ and 5300, together with the experimental data of Toonder
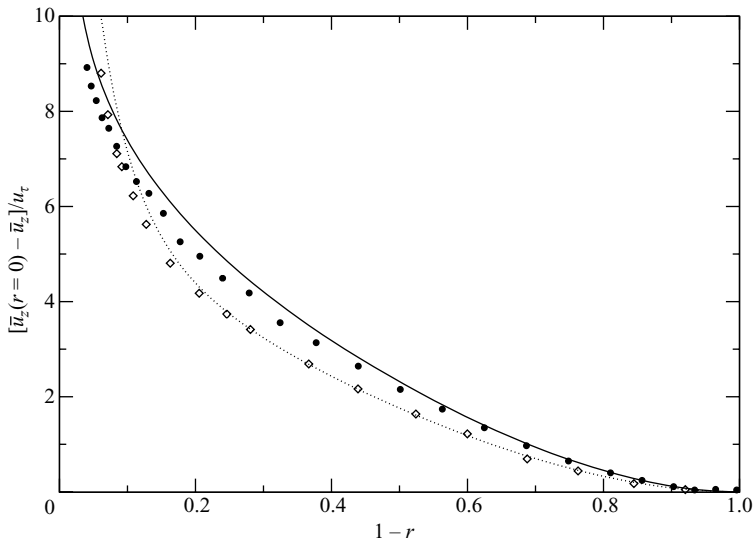
FIGURE 11. Mean velocity defect $[\bar{u}_z(r=0) - \bar{u}_z]/u_\tau$ as a function of $(1-r)$. Solid line: present DNS at $Re_D = 44\,000$; dotted line: present DNS at $Re_D = 5300$; circle: Zagarola & Smits (1998) at $Re_D = 41\,727$; diamond: Durst *et al* (1995) at $Re_D = 7442$.
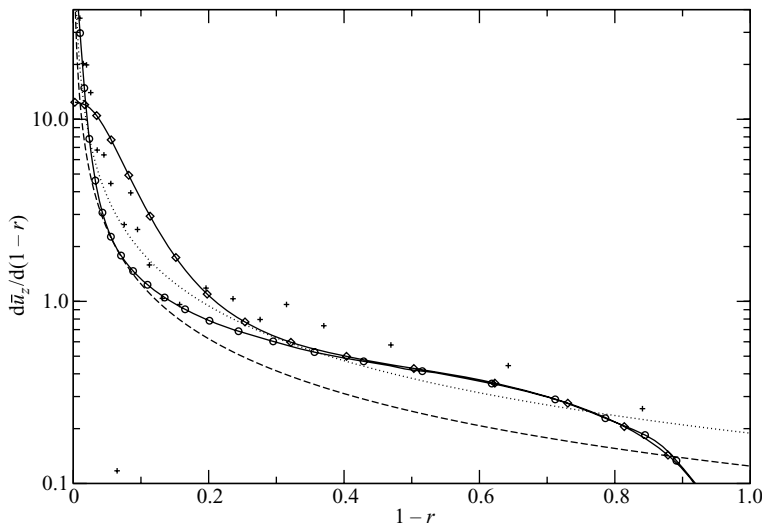

FIGURE 12. Mean velocity gradient $d\bar{u}_z/d(1-r)$ as a function of $(1-r)$. Solid line with circle: present DNS at $Re_D = 44\,000$; solid line with diamond: present DNS at $Re_D = 5300$; dashed line: hyperbolic curve $2.35u_\tau/(1-r)$ at $Re_D = 44\,000$; dotted line: hyperbolic curve $2.76u_\tau/(1-r)$ at $Re_D = 5300$; plus: Toonder & Nieuwstadt (1997) at $Re_D = 24\,580$.

& Nieuwstadt (1997) at $Re_D = 24\,580$. Apparently it is a challenge to obtain smooth experimental mean velocity gradient data. In turbulent pipe flow starting from the wall, the radial profile of $d\bar{u}_z/d(1-r)$ experiences convex-to-concave and concave-to-convex curvature changes. Right at the pipe surface $d\bar{u}_z/d(1-r)$ has a narrow plateau because inside the viscous sublayer mean velocity gradient is constant. For example, the narrow plateau at $Re_D = 44\,000$ has a value of 59.3 at the wall. This
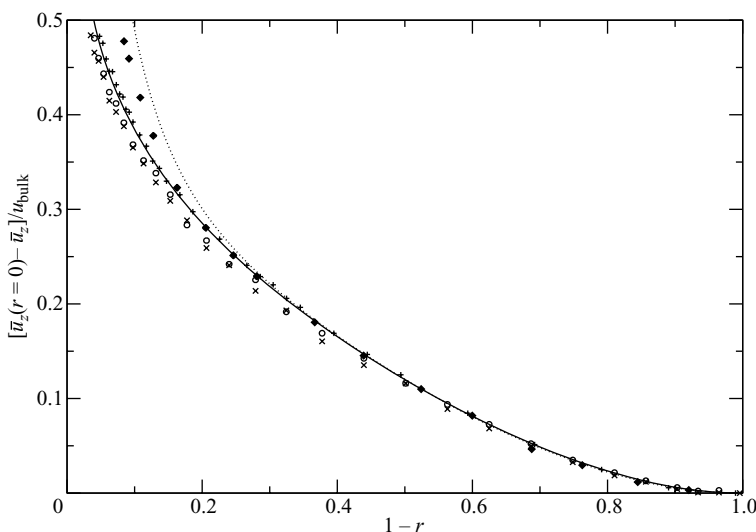
FIGURE 13. Mean velocity defect $[\bar{u}_z(r=0) - \bar{u}_z]/\bar{u}_{bulk}$ as a function of $(1-r)$. Solid line: present DNS at $Re_D = 44\,000$; dotted line: present DNS at $Re_D = 5300$; circle: Zagarola & Smits (1998) at $Re_D = 31\,577$; cross: Zagarola & Smits (1998) at $Re_D = 41\,727$; diamond: Durst *et al.* (1995) at $Re_D = 7442$; plus: Toonder & Nieuwstadt (1997) at $Re_D = 24\,580$.

results in a convex curvature in the immediate vicinity of the wall when viewed from origin of figure 12. In the central portion of the pipe flow between the wall and the pipe axis there is a region within which the radial variation of $\mathrm{d}\bar{u}_z/\mathrm{d}(1-r)$ is rather small. In order for a continuous, monotonically decreasing curve that begins with a very narrow convex plateau to achieve such a slow radial variation in the core region, the profile must experience a concave curvature as shown in the figure. At the pipe axis $\mathrm{d}\bar{u}_z/\mathrm{d}(1-r)$ vanishes. To satisfy this constraint the radial profile must subsequently transition from concave to convex as the pipe axis is approached. Also shown in the figure are curves of $2.35u_\tau/(1-r)$ for $Re_D = 44\,000$ and $2.76u_\tau/(1-r)$ for $Re_D = 5300$. They are tangent to the corresponding $-\mathrm{d}\bar{u}_z/\mathrm{d}r$ profile at a point in the concave segment. The family of hyperbolic concave curve const./$(1-r)$ asymptotes the two coordinate axes. The degree of concaveness and the asymptotic rate depend upon the constant. It is also very interesting to note from figure 12 that for $1-r > 0.4$ the gradient $\mathrm{d}\bar{u}_z/\mathrm{d}(1-r)$ at $Re_D = 44\,000$ and at $Re_D = 5300$ nearly collapse, suggesting that in the pipe central region $\mathrm{d}\bar{u}_z/\mathrm{d}(1-r)$ can be considered as a function of radius only with weak Reynolds number dependence. The collapse of mean velocity gradient in figure 12 suggests that the mean velocity defect profiles for $5300 < Re_D < 44\,000$ should also collapse when normalized by the default unit velocity scale $\bar{u}_{bulk}$. This is verified and confirmed in figure 13 using the present results and four sets of experimental data in the same low-Reynolds-number range. Zagarola & Smits (1998) proposed scaling the mean velocity defect with $\bar{u}_z(r=0) - \bar{u}_{bulk}$. We found that their scaling works reasonably well for the four sets of data in figure 13 with $Re_D > 24\,580$.

4.3. *Comparison with existing theories*

The theory put forward by Wosnik *et al.* (2000) argues in favour of a logarithmic mean velocity distribution inside a mesolayer between $30 < (1-r)^+ < 300$ for all Reynolds numbers if a suitable parameter a^+ is added to $(1-r)^+$. They reported
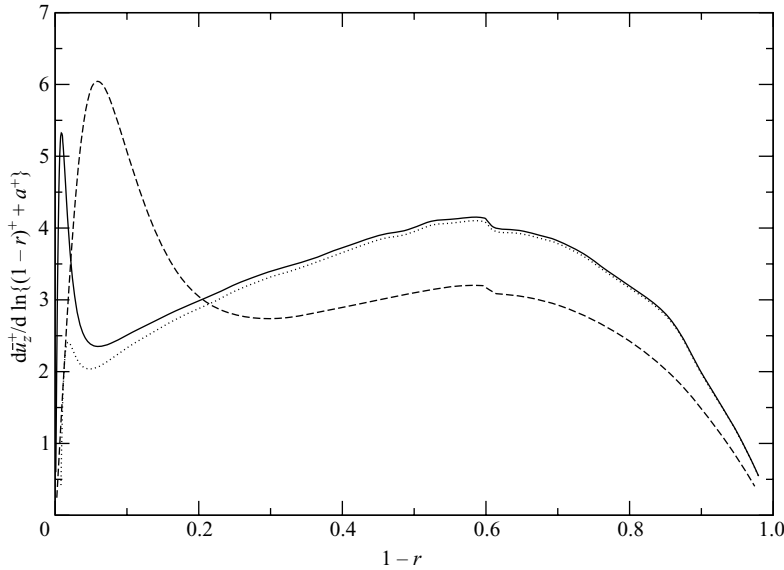
FIGURE 14. Distribution of $\mathrm{d}\overline{u}_z^+/\mathrm{d}\ln\{(1-r)^+ + a^+\}$ as a function of $(1-r)$ from the present DNS. Solid line: $a^+ = 0$ at $Re_D = 44\,000$; dotted line: $a^+ = -8$ at $Re_D = 44\,000$; dashed line: $a^+ = 0$ at $Re_D = 5300$.

that existing DNS and experimental data for $180 < R^+ < 5.3 \times 10^5$ are in agreement with the theory. In figure 14 the gradient of $\overline{u}_z^+$ with respect to $\ln\{(1-r)^+ + a^+\}$ is plotted as a function of $(1-r)$. A blip located near $(1-r) = 0.6$ is seen in figure 14 for both Reynolds numbers. In sections on computational details we reported that the maximum wall-normal grid spacing is located at $r = 0.4087$ for $Re_D = 5300$ and $r = 0.4062$ for $Re_D = 44\,000$. The blip is associated with the piecewise-linear grid point distribution along the radial direction. It is not visible in the velocity gradient diagram of figure 12 but accentuated in the current scale. The overall variation has two ascending and two descending portions with one sharp peak and two gently inflectional regions. At the higher Reynolds number, starting from the wall $\mathrm{d}\overline{u}_z^+/\mathrm{d}\ln(1-r)^+ = (1-r)^+ \mathrm{d}\overline{u}_z^+/\mathrm{d}(1-r)^+$ increases from 0 at the wall to the first peak around $(1-r)^+ = 10$. This ascent can be explained with the usual law of the wall $\overline{u}_z^+ = (1-r)^+$ inside the viscous sublayer. Because $\mathrm{d}\overline{u}_z^+/\mathrm{d}(1-r)^+$ is constant the product has to increase linearly with $(1-r)^+$. For the standard case of $a^+ = 0$ at $Re_D = 44\,000$, within the narrow range of $50 < (1-r)^+ < 90$, $\mathrm{d}\overline{u}_z^+/\mathrm{d}\ln(1-r)^+$ attains a local minimum and varies slowly between 2.4 and 2.35, and may therefore be considered to be approximately constant. At $Re_D = 5300$ there exists a short region of $40 < (1-r)^+ < 80$ with a local minimum value of 2.76 in $\mathrm{d}\overline{u}_z^+/\mathrm{d}\ln(1-r)^+$. Figure 14 also shows that for the case of $a^+ = -8$ as suggested by Wosnik *et al.* (2000), the narrow constant $\mathrm{d}\overline{u}_z^+/\mathrm{d}[\ln(1-r)^+ + a^+]$ region merely shifts closer to the wall. At $a^+ = -16$ the constant region disappears.

In figure 15 we plot $\mathrm{d}\ln\overline{u}_z^+/\mathrm{d}\ln(1-r)^+$ as a function of $(1-r)$ from the present DNS at $Re_D = 44\,000$ tand 5300. The overall variation is qualitatively similar to those shown in figure 14 with two ascending and two descending regions. At the higher Reynolds number the profile attains a near-constant value of 0.149 only within a very narrow region of $70 < (1-r)^+ < 120$. We therefore conclude that the current mean velocity results at $Re_D = 44\,000$ exhibit limited rather than extended power-type behaviour.
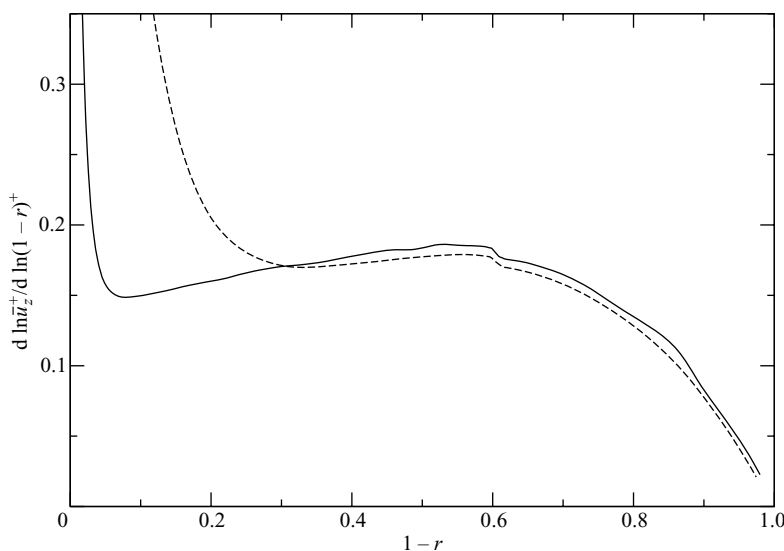
FIGURE 15. Distribution of $\mathrm{d}\ln\overline{u}_z^+/\mathrm{d}\ln(1-r)^+$ as a function of $(1-r)$ from the present DNS. Solid line: $Re_D = 44\,000$; dashed line: $Re_D = 5300$.

4.4. *Rationale for logarithmic $\overline{u}_z^+$ at low Reynolds numbers*

Over the narrow range of $(1-r)^+ = 50$ to 90, the present $\overline{u}_z^+$ at $Re_D = 44\,000$ can be approximated by a logarithmic formula with respect to $(1-r)^+$. This is consistent with previous low-Reynolds-number DNS channel and pipe flow studies. However, it is important to emphasize that this narrow logarithmic slope region is not the one implied by the classical complete similarity logarithmic scaling law. Universal velocity defect law does not hold at such low-Reynolds-number flows, and there is a lack of distinct separation between inner and outer length scales. A number of recent pipe flow studies (Zagarola *et al.* 1997, McKeon *et al.* 2004a, Perry *et al.* 2001, Barenblatt *et al.* 1997) rule out the applicability of a logarithmic scaling theory for low-Reynolds-number flows in which $R^+ < 5000$. The question then arises whether the logarithmic slope region found in flows with Reynolds number as low as $R^+ = 180$ is a mere coincidence with a power-type profile or a physical necessity dictated by the flow. We provide the following two somewhat related rationales. First of all, based on the discussions on figure 12 there is little doubt that the radial profile of $\mathrm{d}\overline{u}_z^+/\mathrm{d}(1-r)^+$ consists of a narrow convex plateau, an extended concave portion, and a final convex segment. It is trivial to show that one can always find a constant such that the concave, hyperbolic curve $\mathrm{const}/(1-r)^+$ is tangent to the concave segment of the velocity gradient at some point. The near-equality of $\mathrm{const}/(1-r)^+$ and $\mathrm{d}\overline{u}_z^+/\mathrm{d}(1-r)^+$ near the tangent point translates into a logarithmic dependence of $\overline{u}_z^+$ on $(1-r)^+$ inside this region. The constant is directly related to the slope of the logarithmic profile. A higher value of the constant results in a less steep concave hyperbolic curve and slower asymptotic rate to the two axes: see figure 12. This easily explains the dependence of the Kármán constant $1/\kappa$ on Reynolds number 2.76 at $R^+ = 180$ and 2.35 at $R^+ = 1142$. Of course, this reasoning does not rule out the possibility of multiple tangent points between $\mathrm{const}/(1-r)^+$ and $\mathrm{d}\overline{u}_z^+/\mathrm{d}(1-r)^+$ in the concave segment.

From a slightly different perspective, we can explain the logarithmic mean velocity profile by considering the variation of $\mathrm{d}\overline{u}_z^+/\mathrm{d}\ln(1-r)^+ = (1-r)^+\mathrm{d}\overline{u}_z^+/\mathrm{d}(1-r)^+$. The
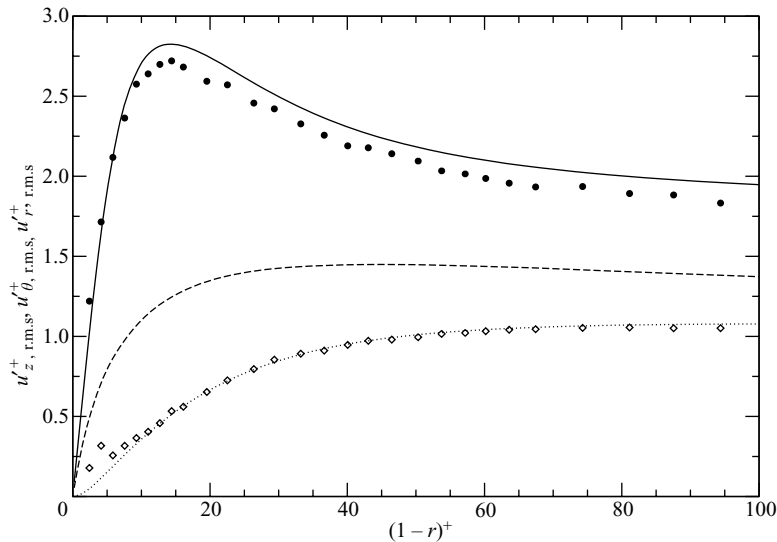
FIGURE 16. Turbulence intensities as a function of $(1-r)^+$ in the near-wall region. Line: present DNS at $Re_D = 44\,000$; symbols: Toonder & Nieuwstadt (1997) at $Re_D = 24\,580$. Solid line: $u'^+_{z,\text{r.m.s.}}$; dashed line: $u'^+_{\theta,\text{r.m.s.}}$; dotted line: $u'^+_{r,\text{r.m.s.}}$.

first descending region in figure 14 together with the second ascending region in turn demands a local minimum of $\mathrm{d}\overline{u}^+_z/\mathrm{d}\ln(1-r)^+$ in-between. A local inflectional minimum region of $\mathrm{d}\overline{u}^+_z/\mathrm{d}\ln(1-r)^+$ would manifest itself as a logarithmic range on a $\overline{u}^+_z$ versus $\ln(1-r)^+$ diagram. The first descent occurs because mean velocity gradient $\mathrm{d}\overline{u}^+_z/\mathrm{d}(1-r)^+$ experiences a precipitous drop slightly away from the wall. Linear increase of the multiplier $(1-r)^+$ is not enough to compensate for the rapid decrease in the mean velocity gradient (figure 12). Away from the immediate vicinity of the wall starting from $(1-r) \approx 0.15$, figure 12 indicates that the precipitous drop of mean velocity gradient is replaced by a mild decrease. Linear increase in the multiplier $(1-r)^+$ over a substantial radial range is now able to compensate the mild decrease of $\mathrm{d}\overline{u}^+_z/\mathrm{d}(1-r)^+$. Therefore, further increase in the value of radial coordinate $1-r$ causes the gradient term $\mathrm{d}\overline{u}^+_z/\mathrm{d}\ln(1-r)^+$ to experience the second ascent. The second descent is because the mean velocity gradient at the pipe axis is zero.

4.5. *Second-order turbulent statistics*

Turbulence intensities normalized by u_τ in the near-wall region are presented in figure 16 together with the data of Toonder & Nieuwstadt (1997) at $Re_D = 24\,580$. The maximum value of $u'^+_{z,\text{r.m.s.}}$ is located in the region of $14 \leqslant (1-r)^+ \leqslant 15$, the same as Laufer's data at a Reynolds number 10 times higher than the present Re_D (Hinze 1975). This is also the peak region reported by Eggels *et al.* (1994) at a Reynolds number only 12 % of the present Re_D. The maximum value of $u'^+_{z,\text{r.m.s.}}$ from the present simulation is 2.82. Morrison *et al.* (2004) reported a large degree of variation in the peak value of $u'^+_{z,\text{r.m.s.}}$ with only a slight change in Reynolds number: from 2.56 at $Re_D = 55\,000$ to 2.93 at $Re_D = 75\,000$. Variations of the three normalized turbulence intensities with the outer coordinate $1-r$ are shown in figure 17. In addition to the data of Toonder & Nieuwstadt, also plotted in the figure are the experimental data of Lawn (1971) at $Re_D = 38\,000$, a Reynolds number close to the present DNS. The comparison is quite satisfactory. Hinze (1975) commented that although the
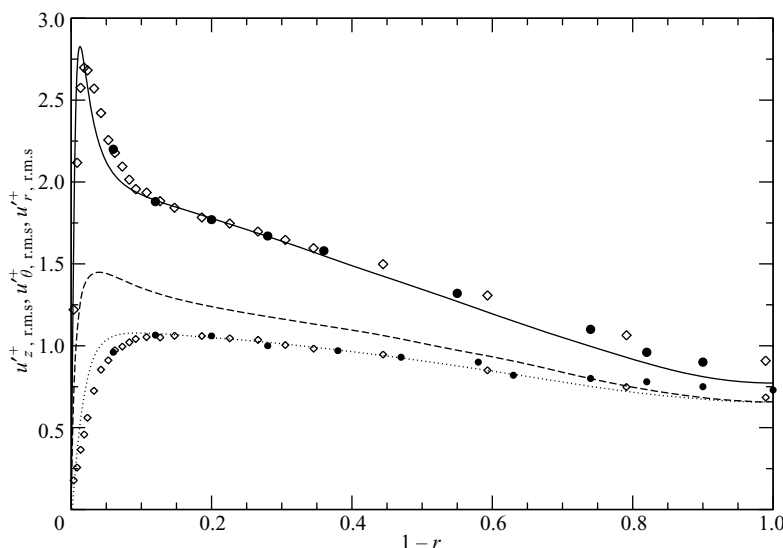
FIGURE 17. Turbulence intensities as a function of $1-r$. Lines: present DNS at $Re_D = 44\,000$; circle: Lawn (1971) at $Re_D = 38\,000$; diamond: Toonder & Nieuwstadt (1997) at $Re_D = 24\,580$. Solid line: $u_{z,\mathrm{r.m.s.}}^{'+}$; dashed line: $u_{\theta,\mathrm{r.m.s.}}^{'+}$; dotted line: $u_{r,\mathrm{r.m.s.}}^{'+}$.

turbulence intensities obtained by Lawn are broadly similar to those of Laufer with a maximum difference of less than 15 %, the main discrepancies are found for data taken near the axis of the pipe rather than near the pipe wall.

In figure 17 the DNS profile of $u_{z,\mathrm{r.m.s.}}^{'}$ bends sharply from $1-r = 0.05$ to 0.1, forming a knee point. Associated with the knee point is a nearly perfect linear distribution of $u_{z,\mathrm{r.m.s.}}^{'}$ with $1-r$ across a substantial radial range $0.15 < 1-r < 0.7$. From $1-r = 0.9$ to the pipe centreline $u_{z,\mathrm{r.m.s.}}^{'}$ has very small variation with radial distance. The averaged curve of $u_{z,\mathrm{r.m.s.}}^{'}$ given by Lawn (1971) from his experimental data on pipe flow at several different Reynolds numbers is also a nearly perfect straight line in the region of $0.1 < 1-r < 0.8$; see the figure 5 of Lawn (1971). The linear dependence of $u_{z,\mathrm{r.m.s.}}^{'}$ on radius only starts to appear when the Reynolds number is above certain relatively low threshold values. For example, the profile at $Re_D = 5300$ shown in figure 2 does not exhibit any indications of knee or linear dependence on $1-r$. The strong linearity of streamwise turbulence intensity in turbulent pipe flow over the region of $0.15 < 1-r < 0.7$ is reinforced by figure 18, in which the present results are plotted together with the experimental data of Perry *et al.* (1986) from $Re_D = 75\,000$ to $200\,000$. Data from Morrison *et al.* (2004) are also shown in the figure. The existence of such a linear axial turbulence intensity profile over a significant portion of pipe cross-section may have been overlooked in previous turbulent pipe flow studies. The appearance of knee points in turbulence intensity profiles is suggestive of distinctive structural zones. See the recent study of Wu *et al.* (2006) and references therein on knee points and the related concept of internal layer. Note that the internal layer concept is applicable only for developing non-equilibrium flows in which the mean velocity is inflectional due to the imposition and relaxation of strong perturbations. In equilibrium-fully-developed-turbulent pipe flow the mean velocity profile is of course not inflectional. But at moderately high Reynolds numbers the wall-normal gradient of mean velocity possesses a strong bending where the sharp drop of $\mathrm{d}\bar{u}_z/\mathrm{d}(1-r)$ with
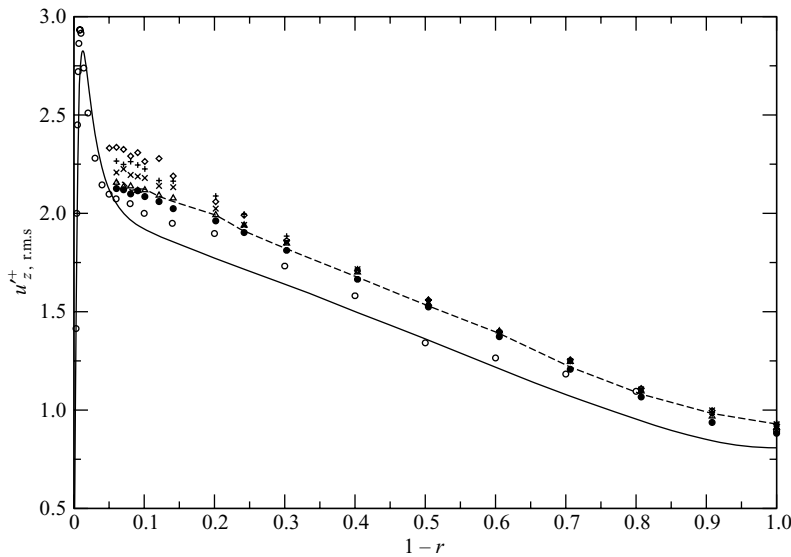
FIGURE 18. Axial turbulence intensity as a function of $1 - r$. Solid line: present DNS at $Re_D = 44\,000$; open circle: Morrison *et al.* (2004) at $Re_D = 75\,000$; all other line and symbols: Perry *et al.* (1986) from $Re_D = 75\,000$ (solid circle) to $Re_D = 200\,000$ (diamond).
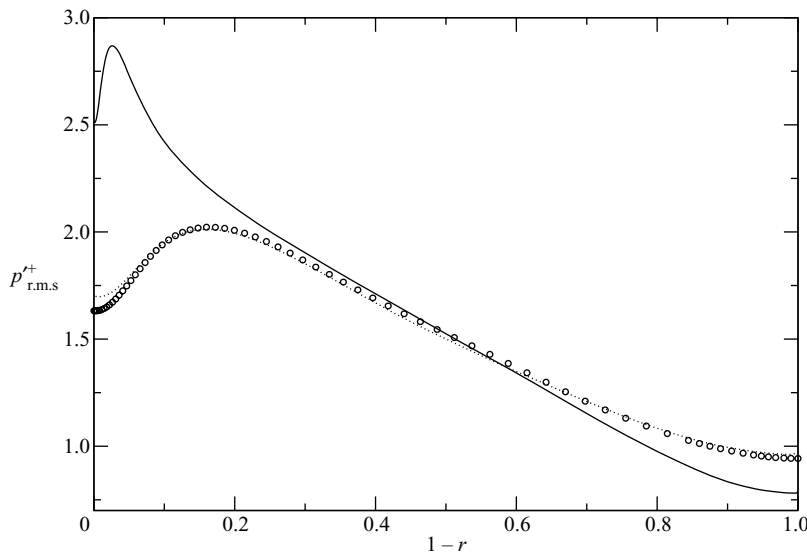

FIGURE 19. Intensity of pressure fluctuation $p'^+_{\text{r.m.s.}}$ as a function of $(1-r)$ from the present DNS. Solid line: $Re_D = 44\,000$; dotted line: $Re_D = 5300$; circle: Loulou *et al.* (1997) at $Re_D = 5600$.

radius is replaced by a more gentle decrease: see figure 12. Statistically this corresponds to the location of knee point in $u'_{z,\text{r.m.s.}}(r)$. In this sense, the enhanced distinctiveness of the wall layer in fully developed pipe flow with increasing Reynolds number bears a certain resemblance to an internal layer found in non-equilibrium flows.

Figure 19 shows the intensity of pressure fluctuation $p'^+_{\text{r.m.s.}}$ as a function of $(1-r)$ from the present study. With the increase of Reynolds number from 5300 to 44\,000 the wall value changes from 1.7 to 2.5, and the peak location also shifts towards
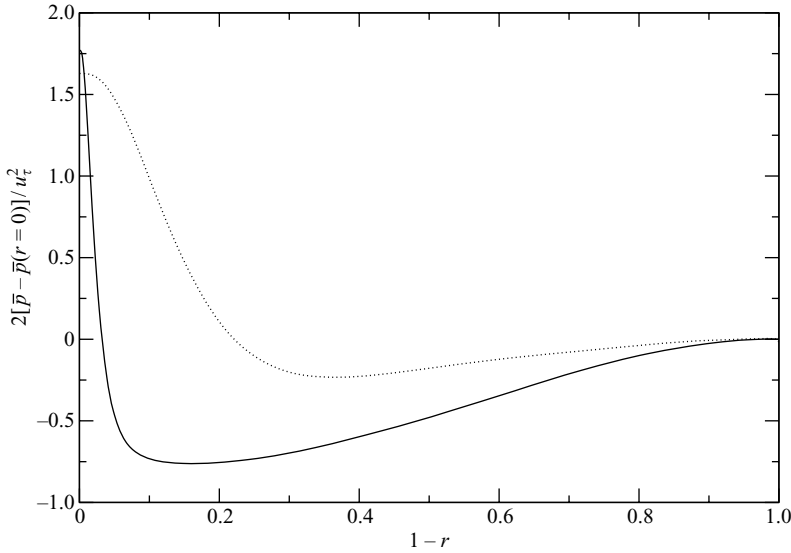
FIGURE 20. Mean pressure $2\left[\overline{p} - \overline{p}(r=0)\right]/u_\tau^2$ as a function of $(1-r)$ from the present DNS; Solid line: $Re_D = 44\,000$; dotted line: $Re_D = 5300$.

the wall. The present results at the lower Reynolds number agree well with those of Loulou *et al.* (1997). Equation (4.2) suggests that mean pressure distribution along the radial direction is important for the analysis of momentum transport. The normalized mean pressure $2[\overline{p} - \overline{p}(r=0)]/u_\tau^2$ as a function of $(1-r)$ is plotted in figure 20 with the reference pressure located at the pipe axis. As indicated in the figure, there is a sharp radial pressure gradient close to the wall. At $Re_D = 44\,000$, mean pressure is the lowest in the region of $0.1 < 1 - r < 0.2$. From there the mean pressure increases monotonically towards the wall and towards the pipe axis. The symmetry condition at the pipe axis is satisfied reasonably well with negligible pressure gradient. It is also evident from figures 19 and 20 that the peak of r.m.s pressure fluctuation is located in the region with the highest mean radial pressure gradient. The offset of peak r.m.s pressure fluctuation location away from the wall is simply due to the fact that mean radial pressure gradient at the wall is small.

Turbulent and viscous shear-stress profiles are presented in figures 21 and 22. Convergence history of the statistics is also shown. Based on the results, it was found that the ratio between turbulence shear stress and turbulence kinetic energy $\overline{u_z' u_r'}/\overline{q^2}$ has a plateau of 0.136 across the range of $0.1 < 1 - r < 0.55$; the ratio of turbulence shear stress to mean velocity gradient $\overline{u_z' u_r'}/[\mathrm{d}\overline{u}_z/\mathrm{d}(1-r)]$ attains a maximum value 0.0033 at $1 - r = 0.4$. Although the present turbulence intensities at $Re_D = 44\,000$ differ little from the data of Toonder & Nieuwstadt (1997) at $Re_D = 24\,580$ (figure 17), there is a substantial variation of turbulent shear-stress profiles at these two Reynolds numbers.

4.6. *Budgets for the mean flow transport equations*

Detailed data on budget terms of the mean momentum transport equations are useful in theoretical studies on mean pipe flow velocity profile. Distributions of the individual terms appearing in equation (4.1) for the $\overline{u}_z$ transport equation are shown in figure 23 at $Re_D = 44\,000$. The residual balance of all the terms was already presented
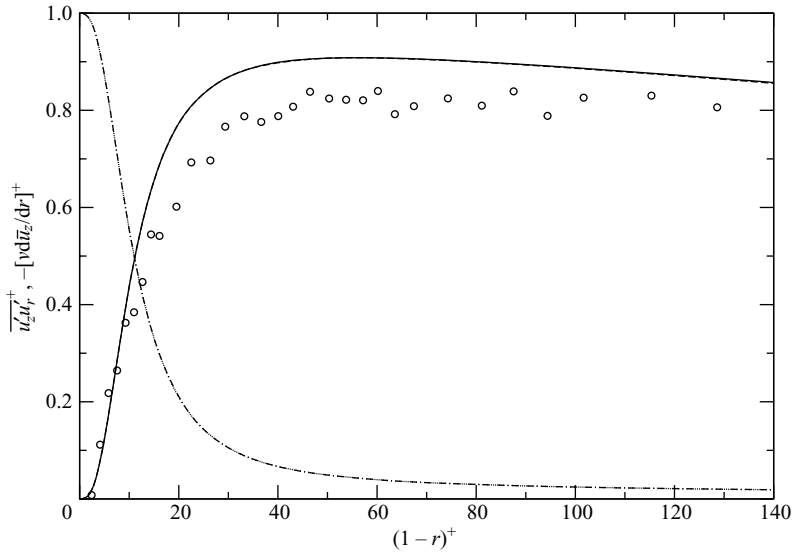
FIGURE 21. Turbulent and viscous shear stresses as a function of $(1-r)^+$ in the near-wall region. Lines: present DNS at $Re_D = 44\,000$; circle: Toonder & Nieuwstadt (1997) at $Re_D = 24\,580$. Solid line: $\overline{u'_z u'_r}^+$ (sampled from $20\,000\Delta t$ to $50\,000\Delta t$); dashed line: $\overline{u'_z u'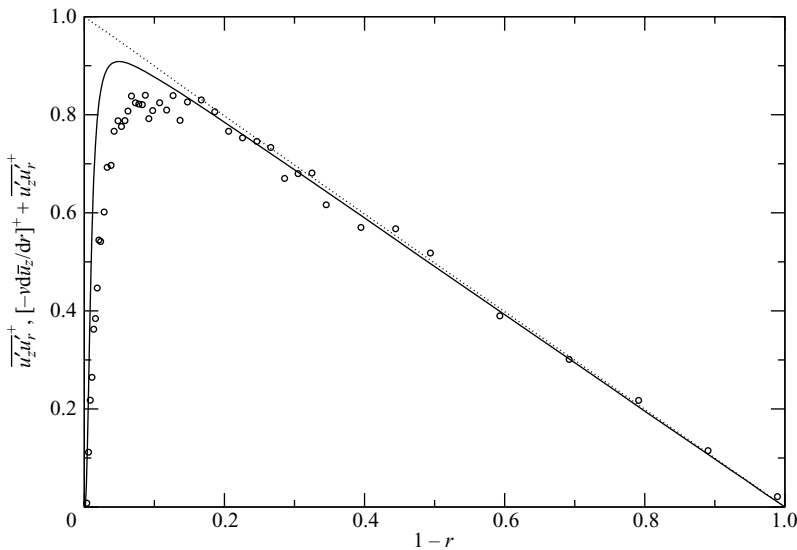_r}^+$ (sampled from $20\,000\Delta t$ to $40\,000\Delta t$); dotted line: $-[\nu d\overline{u}_z/dr]^+$ (sampled from $20\,000\Delta t$ to $50\,000\Delta t$); chain-dotted line: $-[\nu d\overline{u}_z/dr]^+$ (sampled from $20\,000\Delta t$ to $40\,000\Delta t$).

FIGURE 22. Turbulent and total shear stresses as a function of $1-r$. Lines: present DNS at $Re_D = 44\,000$; circle: Toonder & Nieuwstadt (1997) at $Re_D = 24\,580$. Solid line: $\overline{u'_z u'_r}^+$; dotted line: $[-\nu d\overline{u}_z/dr]^+ + \overline{u'_z u'_r}^+$.
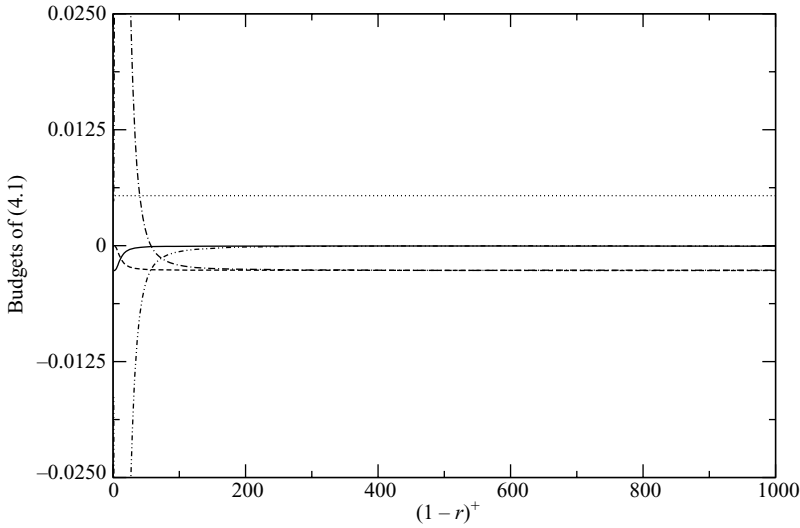
FIGURE 23. Budgets in the $\bar{u}_z$ transport equation (4.1) at $Re_D = 44\,000$. Dotted line: $-(1/\rho)\partial\bar{p}/\partial x$; solid line: $(\nu/r)(d\bar{u}_z/dr)$; chain-dotted-dotted line: $\nu d^2\bar{u}_z/dr^2$; dashed line: $-\overline{u'_z u'_r}/r$; chain-dotted line: $-d\overline{u'_z u'_r}/dr$. Normalization is with respect to $\bar{u}^2_{bulk}/R$.

in figure 6 and the absolute maximum error is $7.82 \times 10^{-5}\bar{u}^2_{bulk}/R$. We found that in the region of $3 < (1-r)^+ < 15$, the viscous term and the turbulent shear-stress term $-d\overline{u'_z u'_r}/dr$ dominate other contributions. Very close to the wall $(1-r)^+ < 2$, all the terms in equation (4.1) are important except for the turbulent shear-stress curvature term $-\overline{u'_z u'_r}/r$. In particular, contribution from the viscous shear-stress curvature term $(\nu/r)d\bar{u}_z/dr$ is not negligible. However, this term is only important below $(1-r)^+ = 30$. Within the range of $30 < (1-r)^+ < 200$ all the remaining four terms are important, i.e. axial pressure gradient, gradient of viscous shear-stress, gradient of turbulent shear-stress, and the turbulent shear-stress curvature term. Beyond $(1-r)^+ = 200$, contribution from the gradient of viscous shear-stress becomes negligible and only the remaining three terms are important. It is clear from figure 23 that the magnitude of the turbulent shear-stress curvature term $-\overline{u'_z u'_r}/r$ is nearly the same as the magnitude of the gradient of turbulent shear stress $-d\overline{u'_z u'_r}/dr$ over most of the pipe cross-section for $(1-r)^+ > 200$. This is to be expected because of the nearly linear distribution of $\overline{u'_z u'_r}$ shown in figure 22. By $(1-r)^+ = 200$, all the terms appearing in equation (4.1) have attained their corresponding asymptotic values, and there are almost no further variations across the wide range of $(1-r)^+ > 200$. Again, this is dictated by the viscous and turbulent shear-stress distributions in fully developed turbulent pipe flow.

Budgets for the $\bar{u}_z$ transport equation at $Re_D = 5300$ are given in figure 24 and the trends are qualitatively analogous to those at the higher Reynolds number. The budget term results obtained from present DNS paint a more complicated picture than assumed in some existing simplified models. The three budget terms appearing in (4.2) for the radial momentum balance were also evaluated. The contribution from the anisotropy curvature term $-(\overline{u'^2_r} - \overline{u'^2_\theta})/r$ is small for most of the pipe cross-section. The transport equation for $\bar{u}_r$ is balanced mostly by the radial gradient of mean pressure and the gradient of turbulence fluctuations in the radial direction $-d\overline{u'^2_r}/dr$.
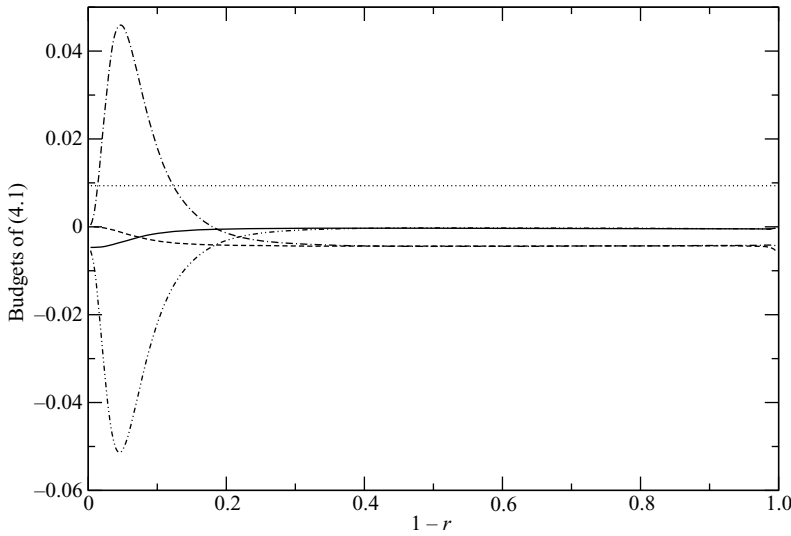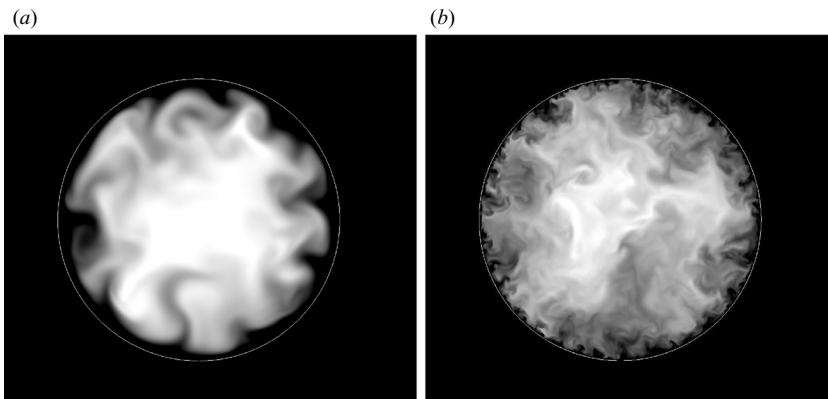
FIGURE 24. Budgets in the $\bar{u}_z$ transport equation (4.1) as a function of $(1-r)$ at $Re_D = 5300$. Dotted line: $-(1/\rho)\partial\bar{p}/\partial x$; solid line: $(\nu/r)(\mathrm{d}\bar{u}_z/\mathrm{d}r)$; chain-dotted-dotted line: $\nu\mathrm{d}^2\bar{u}_z/\mathrm{d}r^2$; dashed line: $-\overline{u'_z u'_r}/r$; chain-dotted line: $-\mathrm{d}\overline{u'_z u'_r}/\mathrm{d}r$. Normalization is with respect to $\bar{u}^2_{bulk}/R$.

FIGURE 25. Visualization of the turbulent pipe flow over constant z plane using contours of instantaneous u_z. (a) $Re_D = 5300$; (b) $Re_D = 44\,000$. White represents higher values of u_z.

5. Visualizations at $Re_D = 5300$ and $Re_D = 44\,000$

Given the canonical nature and fundamental importance of turbulent pipe flow, it is interesting to note that there have been few published turbulent pipe flow visualizations from either experiment or DNS. A case in point is van Dyke's *An Album of Fluid Motion*, in which the only pipe flow image is a repetition of Reynolds' dye experiment for a transitional tube flow. Here we present a set of images extracted from our DNS restart data files for the two Reynolds numbers, $Re_D = 5300$ and $Re_D = 44\,000$. These images were produced in a straightforward manner by plotting flooded contours of instantaneous axial velocity u_z over selected surfaces of constant coordinates in the cylindrical system. No other elaborate visualization or post-processing procedures were used. At each Reynolds number the presented images are at the same instant. Figure 25 compares the contours over a constant z plane
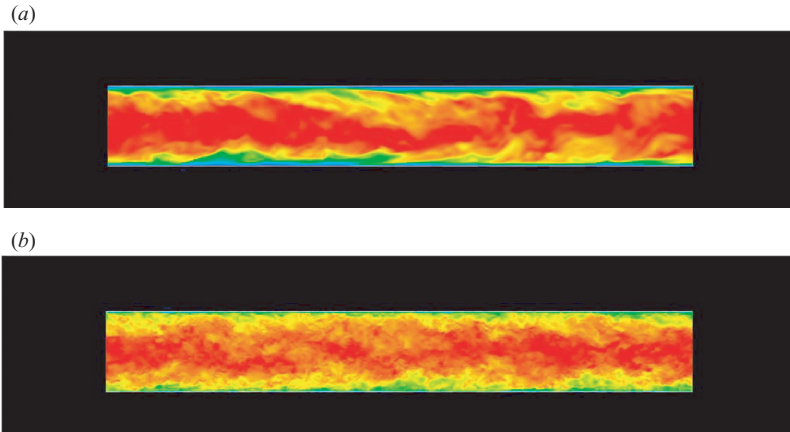
(a)

(b)

FIGURE 26. Visualization of the turbulent pipe flow over constant θ plane using contours of instantaneous u_z. (a) $Re_D = 5300$; (b) $Re_D = 44\,000$. Red represents higher values of u_z.

at the two Reynolds numbers. A total of 160 grey scales were used in this figure to represent the magnitude of u_z from 0.6 (black) to 1.3 (white). The image at the low Reynolds number exhibits large-scale bright-coloured high-momentum blobs and dark-coloured low-momentum fluid lumps jigsawed along the azimuthal direction. These structures occupy sizable regions over the (r, θ) cross-section and some of them have a vague mushroom shape. As expected, the contours in figure 25 at $Re_D = 44\,000$ exhibit much more fine-grain structures. The alternation of high- and low-momentum fluid blobs are still visible but with reduced apparent coherence. It was found that within a reasonable range the visualized structures do not depend upon the exact threshold levels for the contours.

Figures 26 compares contours of u_z over the constant θ plane at $Re_D = 5300$ and $Re_D = 44\,000$. The entire streamwise range of the computational domain $0 \leqslant z \leqslant 15$ is included. At the lower Reynolds number there are wavy low-momentum fluid structures inclined away from the wall towards the downstream direction. In the pipe central region there are blobs of higher-speed wavy structures elongated along the axial direction. The structures at $Re_D = 44\,000$ are less coherent in the figure. Figures 27 and 28 present contours of u_z over constant r surfaces at $1 - r = 0.01$ and 0.1 for both Reynolds numbers. Only one out of every four adjacent grid points along the streamwise z direction was used in producing the $Re_D = 44\,000$ images shown in these two figures. All the 1024 grid points along the θ direction are displayed. At $Re_D = 5300$ the two images for $1 - r = 0.01$ and 0.1 exhibit consistent footprints of high-momentum structures elongated and twisted in the streamwise direction. The coherence in the radial and azimuthal directions of these large-scale structures is rather clear. It is very likely that these contour surfaces are signatures of the same set of coherent structures. At the higher Reynolds number figure 27(b) reveals a large number of worm-like elongated high-momentum structures with very narrow azimuthal dimension. Streamwise dimensions of these elongated structures appear to be less than those at $Re_D = 5300$.

6. Correlations at $Re_D = 5300$ and $Re_D = 44\,000$

One question in association with the comparison of visualization images between $Re_D = 5300$ and $Re_D = 44\,000$ in the previous section is that whether the
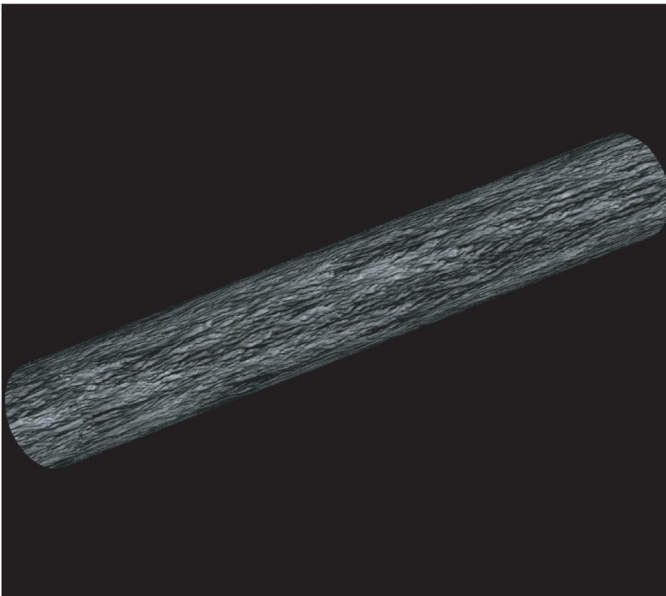
(*a*)
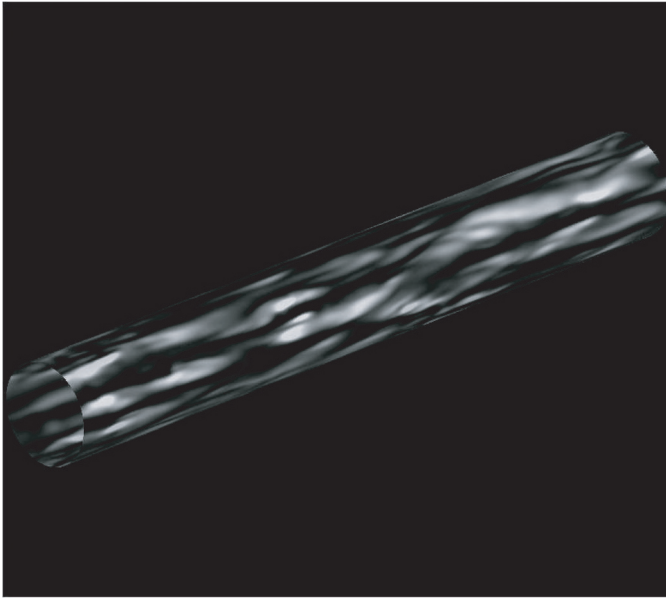
(*b*)

FIGURE 27. Visualization of the turbulent pipe flow over the surface of $1 - r = 0.01$ using contours of instantaneous u_z. White represents higher values of u_z. (*a*) $Re_D = 5300$. (*b*) $Re_D = 44\,000$.

non-dimensional extent of large structures has been reduced at the higher Reynolds number or the apparent reduced coherence in absolute scale is just a simple manifestation of scaling. This can be more fully addressed with two-point correlation results.
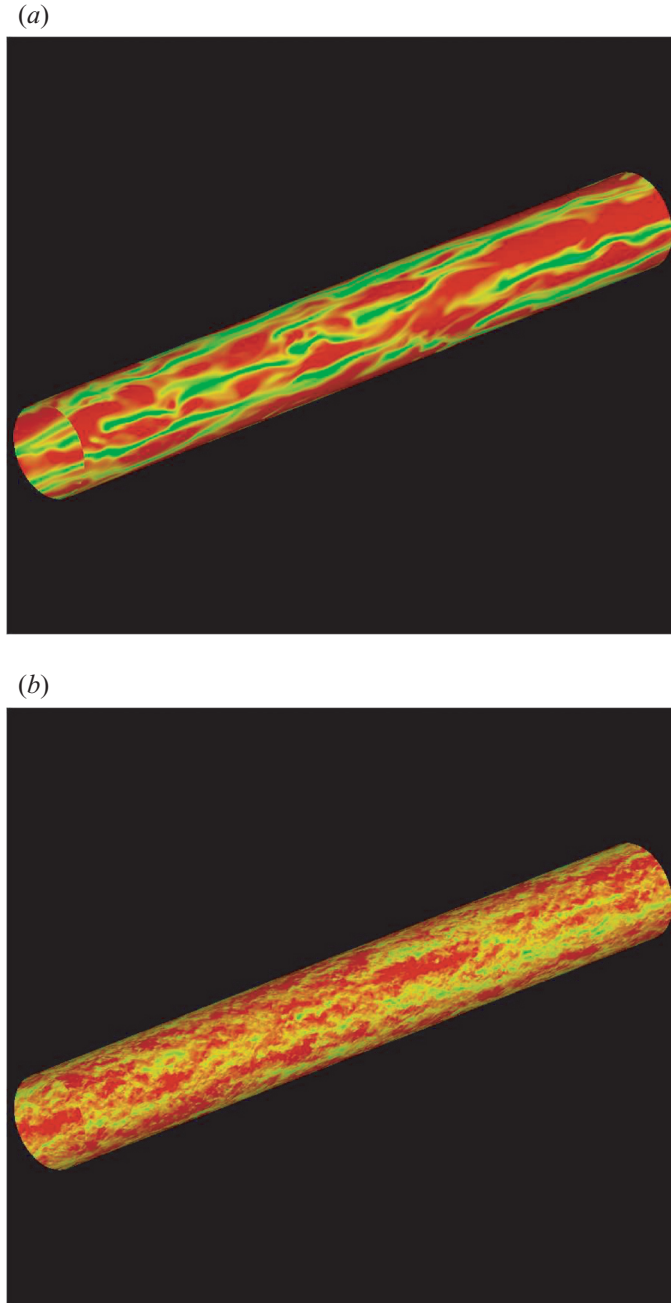
(*a*)

(*b*)

FIGURE 28. Visualization of the turbulent pipe flow over the surface of $1 - r = 0.1$ using contours of instantaneous u_z. Red represents higher values of u_z. (*a*) $Re_D = 5300$. (*b*) $Re_D = 44\,000$.

The two-point correlation coefficient $R_{u'_z u'_z}$ as a function of streamwise separation $z - z'$ at five radial positions is shown in figure 29 for $Re_D = 5300$ and in figure 30 for $Re_D = 44\,000$, respectively. The results suggest a different dependence on $1 - r$ for the two Reynolds numbers. At $Re_D = 5300$ the correlation decreases with increasing radial
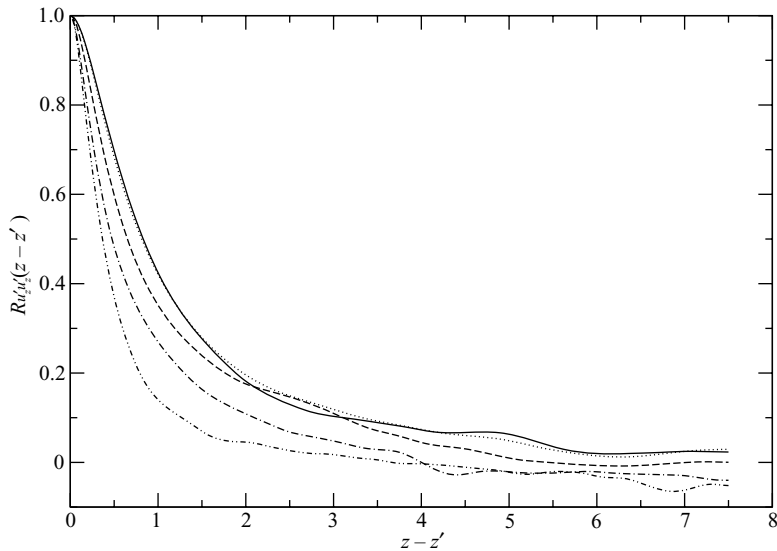
FIGURE 29. Two-point correlation coefficient $R_{u'_z u'_z}$ at $Re_D = 5300$ as a function of the streamwise separation $z - z'$. Solid line: $1 - r = 0.01$; dotted line: $1 - r = 0.05$; dashed line: $1 - r = 0.1$; chain-dotted line: $1 - r = 0.2$; chain-dotted-dotted line: $1 - r = 0.5$.

FIGURE 30. Two-point correlation coefficient $R_{u'_z u'_z}$ at $Re_D = 44\,000$ as a function of the streamwise separation $z - z'$. Solid line: $1 - r = 0.01$; dotted line: $1 - r = 0.05$; dashed line: $1 - r = 0.1$; chain-dotted line: $1 - r = 0.2$; chain-dotted-dotted line: $1 - r = 0.5$.
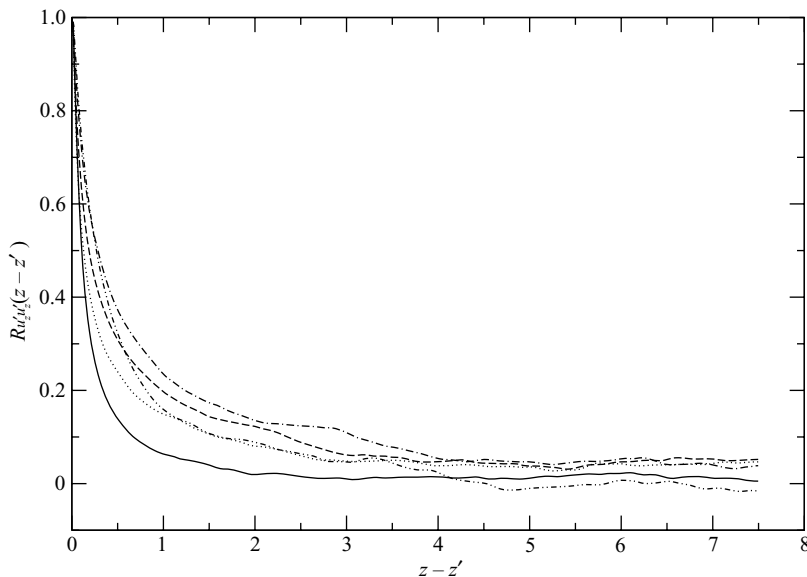
distance from the wall. At $Re_D = 44\,000$ the correlation increases with the change of radial position from $1 - r = 0.01$ to 0.2. From $1 - r = 0.2$ to 0.5, $R_{u'_z u'_z}$ decreases. Thus, at $Re_D = 5$, 300 the two-point streamwise correlation $R_{u'_z u'_z}$ is largest inside the viscous sublayer, but at $Re_D = 44\,000$ it peaks outside the logarithmic layer. From the two
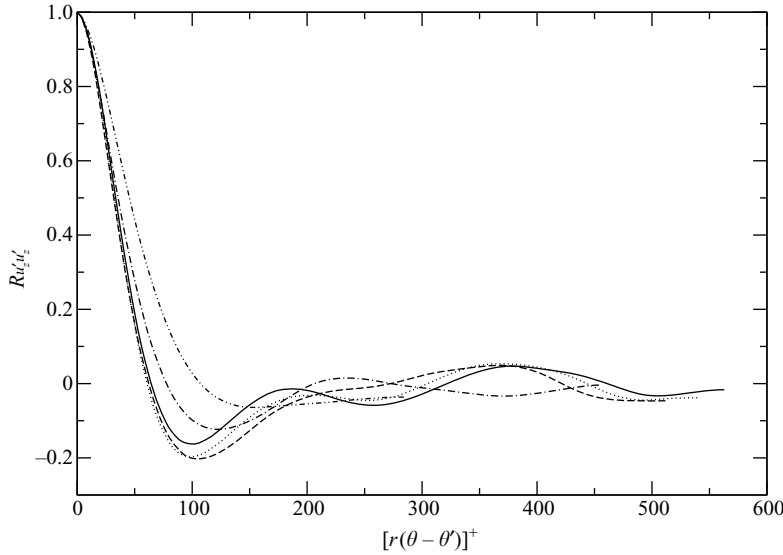
FIGURE 31. Two-point correlation coefficient $R_{u'_z u'_z}$ at $Re_D = 5300$ as a function of local azimuthal separation $[r(\theta - \theta')]^+$. Solid line: $1 - r = 0.01$ $((1 - r)^+ = 1.81)$; dotted line: $1 - r = 0.05$; dashed line: $1 - r = 0.1$; chain-dotted line: $1 - r = 0.2$; chain-dotted-dotted line: $1 - r = 0.5$.

figures it can also be seen that close to the wall at the radial station of $1 - r = 0.01$, $R_{u'_z u'_z}$ drops to values close to zero starting from about $2R$ for $Re_D = 44\,000$ and about $6R$ for $Re_D = 5300$. This is consistent with the images shown in figures 27 in which the axial elongation of near-wall structure at the lower Reynolds number is much prominent than at the higher Reynolds number. For both Reynolds numbers away from the wall at the radial station of $1 - r = 0.5$ the correlation coefficient $R_{u'_z u'_z}$ drops to values close to zero for axial separations larger than approximately $4R$. The streamwise extent of large-scale structures away from the wall in the core region seems to be quite similar at $Re_D = 5300$ and $Re_D = 44\,000$; see also figure 28. Our visualizations and correlations suggest that at $Re_D = 5300$ turbulent pipe flow possesses large-scale, near-wall structures that are coherent over significant axial ($8R$ or larger) and radial dimensions (approximately $0.2R$). These results also indicate that the present computational domain length of $15R$ is adequate.

   Variations of $R_{u'_z u'_z}$ as a function of the azimuthal separation $\theta - \theta'$ are shown in figure 31 for $Re_D = 5300$ and in figure 32 for $Re_D = 44\,000$, respectively. In both figures the azimuthal separation $\theta - \theta'$ is multiplied by the local radial coordinate r and also converted into wall units. Note that at the higher Reynolds number $R(\theta - \theta')^+$ extends to 3588, but only results with separations less than 600 are shown for clarity. For $Re_D = 5300$, the correlation at the radial station of $(1 - r)^+ = 9.05$ attains its first zero value at approximately $r(\theta - \theta')^+ = 70$. For $Re_D = 44\,000$, $R_{u'_z u'_z}$ at the radial station of $(1 - r)^+ = 11.4$ attains its first zero at approximately $r(\theta - \theta')^+ = 65$. This suggests that the drastic difference in azimuthal dimension of the near-wall structures shown in figures 27(a) and figure 27(b) can be attributed mostly to Reynolds number scaling. The curve for $(1 - r)^+ = 11.4$ at the higher Reynolds number stays at values close to zero for separations larger than 100 wall units. In contrast, the curve for $(1 - r)^+ = 9.05$ at the lower Reynolds number displays relatively large-amplitude
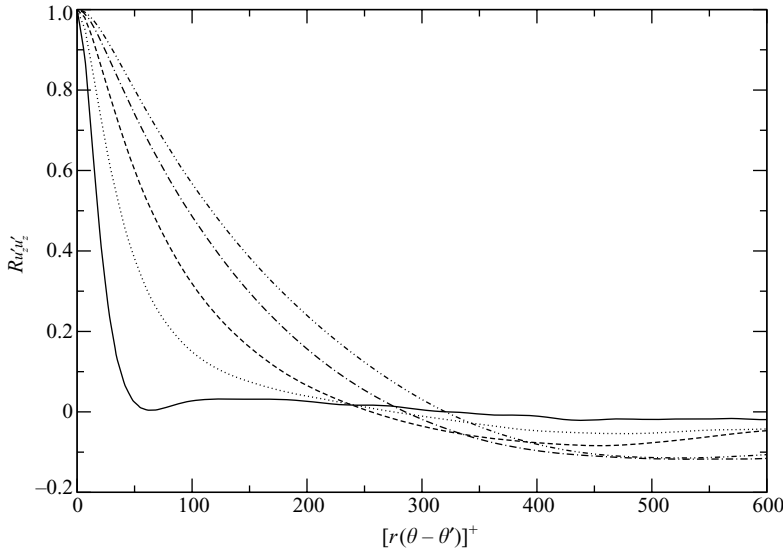
FIGURE 32. Two-point correlation coefficient $R_{u'_z u'_z}$ at $Re_D = 44\,000$ as a function of local azimuthal separation $[r(\theta - \theta')]^+$. Solid line: $1 - r = 0.01$ $((1-r)^+ = 11.4)$; dotted line: $1 - r = 0.05$; dashed line: $1 - r = 0.1$; chain-dotted line: $1 - r = 0.2$; chain-dotted-dotted line: $1 - r = 0.5$. For clarity results for $[r(\theta - \theta')]^+ > 600$ are not shown.

wavy behaviour along the azimuthal direction with secondary peaks. This demonstrates that the coupling or interdependence of the near-wall longitudinal structures along the azimuthal direction is much stronger at $Re_D = 5,300$. Although there is negligible negative peak at $(1-r)^+ = 11.4$ for the higher Reynolds number in figure 32, away from the wall, however, $R_{u'_z u'_z}$ does display a set of deeper negative peaks at larger values of $1 - r$. This suggests a stronger coupling of the longitudinal structures along the azimuthal direction in the outer region at $Re_D = 44\,000$. Figure 31 shows that for $Re_D = 5300$ the correlation at $1 - r = 0.5$ descends to zero from high value at approximately $r(\theta - \theta')^+ = 110$, which translates to an azimuthal scale of $r(\theta - \theta') = 0.61$. Figure 32 shows that for $Re_D = 44\,000$ the correlation at $1 - r = 0.5$ descends to zero from high value at approximately $r(\theta - \theta')^+ = 320$, corresponding to an azimuthal scale of $r(\theta - \theta') = 0.28$.

Bailey *et al.* (2007) reported hot-wire measurements of $R_{u'_z u'_z}$ with azimuthal probe separation in the Princeton Superpipe at four radial positions. They found that within the logarithmic layer the azimuthal length scale in the pipe flow is similar to that in a planar channel, but outside the logarithmic layer the azimuthal length scale in the pipe flow is less than that in a channel flow. The two point correlations at $Re_D = 5300$ shown in figures 29 and 31 are consistent with previous low-Reynolds-number channel flow results, (e.g. Moin & Kim 1982). At $R^+ = 180$, $R_{u'_z u'_z}$ very near the wall has a noticeably larger streamwise correlation distance $z - z'$ compared to that in the central region; $R_{u'_z u'_z}$ with spanwise (azimuthal) separation has a modestly larger correlation distance in the core. For higher-Reynolds-number pipe flows the streamwise coherence of the near-wall worm-like structures is less than the streamwise coherence of the high-momentum elongated wavy structures in the core region, but the trend of the radial variation is not monotonic.

7. Summary

Our large-scale computation of the fully developed, incompressible turbulent flow through at smooth pipe at $Re_D = 44\,000$ demonstrates that direct numerical simulation has achieved a Reynolds number exceeding the lower limit used in the Princeton Superpipe experiments as well as that used in the classical experiment of Lawn (1971). Good agreement was obtained with the Princeton data on mean flow statistics, and with Lawn's data on turbulence intensities. This in turn makes it possible for a less ambiguous connection to the on-going examination on mean pipe flow characteristics.

Our calculated mean velocity gradient results at $Re_D = 44\,000$ suggest that the $\overline{u}_z^+$ profile fits well into a limited rather than extended power-type formula. The present low-Reynolds-number results are not consistent with the theory advanced by Wosnik *et al.* (2000). Furthermore, it was shown that the radial profile of $\mathrm{d}\overline{u}_z^+/\mathrm{d}(1-r)^+$ consists of convex, concave, and convex curvature segments sequentially from the wall. The logarithmic dependence of $\overline{u}_z^+$ on $(1-r)^+$ at very low Re_D may be understood by considering the nature of these curvature segments in relation to the concave hyperbolic curve const.$/(1-r)^+$. Although differing substantially near the wall, profiles of $\mathrm{d}\overline{u}_z/\mathrm{d}(1-r)$ at $Re_D = 44\,000$ and at $Re_D = 5300$ nearly collapse for the central region of $0.4 < 1-r < 1$. Consequently, mean velocity defect profiles within the region of $5300 < Re_D < 44\,000$ also collapse when normalized by the default unit velocity scale $\overline{u}_{bulk}$.

We found that at $Re_D = 44\,000$ the axial turbulent intensity profile possesses one near-wall knee point. The entire radial profile can be divided into three segments: a near-wall peak region for $1-r < 0.1$, a nearly perfect linear variation of $u'_{z,\mathrm{r.m.s.}}$ with radius for $0.15 < 1-r < 0.7$, and an approximately constant $u'_{z,\mathrm{r.m.s.}}$ for $1-r > 0.9$. Existence of knee points may be a symptom of distinctly different structural zones in the flow. Statistically, in equilibrium-wall-bounded turbulent flows, this is related to the strong bending of near-wall mean velocity gradient.

Budgets of the mean velocity balance at $Re_D = 44\,000$ show that only in a very narrow range of approximately 12 wall units do the effects of viscous shear-stress gradient and turbulent shear-stress gradient overwhelm other contributions. As a result of the simple shear-stress profiles in turbulent pipe flow, beyond $(1-r)^+ = 200$ all terms in the mean axial momentum transport equation remain nearly unchanged.

Flow visualization images at $Re_D = 5300$ reveal large near-wall wavy streaky structures that are quite coherent over the axial- $(> 8R)$ and radial- $(> 0.2R)$ directions. These streaks are also noticeably correlated with each other along the azimuthal direction. At $Re_D = 44\,000$ the streamwise extent of these near-wall worm-like streak structures is reduced, but when measured in wall units their azimuthal dimension is still comparable to that at the lower Reynolds number. High-speed wavy structures elongated along the axial direction are seen in the core region of the pipe, and their streamwise and azimuthal dimensions do not change substantially with the increase of Reynolds number from 5300 to 44 000.

The present numerical study at $R^+ = 1142$ has only made a limited connection to the on-going debate regarding mean pipe flow properties. A more substantial connection may be achieved if the simulation Reynolds number can be pushed beyond $R^+ = 5000$ since, according to the theory of Zagarola & Smits (1998), this is the lower threshold for which there appears a logarithmic region in the inertial sublayer. We notice that the highest Re_τ achieved in channel flow DNS at present is the simulation of Hoyas & Jiménez (2006) at $Re_\tau = 2003$. Assuming 600 grid points are clustered along the radial

direction, we estimate the total number of grid points for the $R^+ = 5000$ simulation to be approximately 2.4×10^{10}, about 40 times larger than the current grid size of 630 million. Given the fact that the present simulation was carried out on 1024 processors, the number of processors required for a $R^+ = 5000$ simulation should be around 40 000. This is certainly achievable with the best of today's technology.

The present computational results have been posted on the Stanford University Center for Turbulence Research web site (http://ctr.stanford.edu) for public access.

REFERENCES

AKSELVOLL, K. & MOIN, P. 1996a Large eddy simulation of confined turbulent coaxial jets. *J. Fluid Mech.* **315**, 387–411.

AKSELVOLL, K. & MOIN, P. 1996b An efficient method for temporal integration of the Navier–Stokes equations in confined axisymmetric geometries. *J. Comput. Phys.* **125**, 454–463.

BAILEY, S., HULTMARK, M., SMITS, A. J. & SCHULTZ, M. 2007 Azimuthal correlation in the outer layer of turbulent pipe flow. *Bull. Am. Phys. Soc.* **52**, 24.

BARENBLATT, G. I. & CHORIN, A. J. 1998 Scaling of the intermediate region in wall-bounded turbulence: The power law. *Phys. Fluids* **10**, 1043–1044.

BARENBLATT, G. I., CHORIN, A. J. & PROSTOKISHIN, V. M. 1997 Scaling laws for fully developed turbulent flow in pipes. *Appl. Mech. Rev.* **50**, 413–529.

DURST, F., JOVANOVIC, J. & SENDER, J. 1995 LDA measurements in the near-wall region of a turbulent pipe flow. *J. Fluid Mech.* **295**, 305–335. Data available at http://torroja.dmt.upm.es/ftp/AGARD/.

EGGELS, J. G. M., UNGER, F., WEISS, M. H., WESTERWEEL, J., ADRIAN, R. J., FRIEDRICH, R. & NIEUWSTADT, F. T. M. 1994 Fully developed turbulent pipe flow: A comparison between direct numerical simulation and experiment. *J. Fluid Mech.* **268**, 175–209.

FUKAGATA, K. & KASAGI, N. 2002 Highly energy-conservative finite difference method for the cylindrical coordinate system. *J. Comput. Phys.* **181**, 478–498.

GUALA, M., HOMMEMA, S. E. & ADRIAN, R. J. 2006 Large-scale and very-large-scale motions in turbulent pipe flow, *J. Fluid Mech.* **554**, 521–542.

HINZE, J. O. 1975 *Turbulence.* Second edition. McGraw-Hill.

HOYAS, S. & JIMÉNEZ, J. 2006 Scaling of the velocity fluctuations in turbulent channels up to $Re_\tau = 2003$ *Phys. Fluids* **18**, 011702.

KIM, J. & MOIN, P. 1985 Application of a fractional-step method to incompressible Navier–Stokes equations. *J. Comput. Phys.* **59**, 308–323.

KIM, K. C. & ADRIAN, R. J. 1999 Very-large scale motion in the outer layer. *Phys. Fluids* **11**, 417–422.

LAWN, C. J. 1971 The determination of the rate of dissipation in turbulent pipe flow. *J. Fluid Mech.* **48**, 477–505.

LOULOU, P., MOSER, R. D., MANSOUR, N. N. & CANTWELL, B. J. 1997 Direct numerical simulation of incompressible pipe flow using a B-spline spectral method. *NASA Technical Memo.* Data available at http://torroja.dmt.upm.es/ftp/AGARD/.

MCKEON, B. J., LI, J., JIANG, W., MORRISON, J. F. & SMITS, A. J. 2004a Further observations on the mean velocity distribution in fully developed pipe flow. *J. Fluid Mech.* **501**, 135–147.

McKeon, B. J., Swanson, C. J., Zagarola, M. V., Donnelly, R. J. & Smits, A. J. 2004b Friction factors for smooth pipe flow. *J. Fluid Mech.* **511**, 41–44.

Moin, P. & Kim, J. 1982 Numerical investigation of turbulent channel flow. *J. Fluid Mech.* **118**, 341–377.

Morrison, J. F., McKeon, B. J., Jiang, W. & Smits, A. J. 2004 Scaling of the streamwise velocity component in turbulent pipe flow. *J. Fluid Mech.* **508**, 99–131.

Oberlack, M. 2001 A unified approach for symmetries in plane parallel turbulent shear flows. *J. Fluid Mech.* **427**, 299–328.

Orlandi, P. & Fatica, M. 1997 Direct simulations of turbulent flow in a pipe rotating about its axis. *J. Fluid Mech.* **343**, 43–72.

Perry, A. E., Hafez, S. & Chong, M. S. 2001 A possible reinterpretation of the Princeton Superpipe data. *J. Fluid Mech.* **439**, 395–401.

Perry, A. E., Henbest, S. M. & Chong, M. S. 1986 A theoretical and experimental study of wall turbulence. *J. Fluid Mech.* **165**, 163–199.

Pierce, C. D. & Moin, P. 2001 Progress variable approach for large-eddy simulation of turbulent combustion. *Repo.*TF-80, Stanford University.

Pierce, C. D. & Moin, P. 2004 Progress variable approach for large-eddy simulation of non-premixed turbulent combustion. *J. Fluid Mech.*, **504**, 73–97.

Satake, S., Kunugi, T. & Himeno, R. 2000 High Reynolds number computation for turbulent heat transfer in a pipe flow. *In Lecture Notes in Computer Science*, pp. 514–523. Springer.

Smits, A. J. & Zagarola, M. V. 1998 Response to 'Scaling of the intermediate region in wall-bounded turbulence: The power law'. *Phys. Fluids* **10**, 1045–1046.

Toonder, J. M. J. & Nieuwstadt, F. T. M. 1997 Reynolds number effects in a turbulent pipe flow for low to moderate *Re. Phys. Fluids* **9**, 3401–3409.

Veenman, M. P. B. 2004 Statistical analysis of turbulent pipe flow: numerical approach. Ph.D. thesis, Eindhoven University of Technology, Faculty of Mechanical Engineering.

Wagner, C., Huttl, T. J. & Friedrich, R. 2001 Low Reynolds number effects derived from direct numerical simulations of turbulent pipe flow. *Comput. Fluids* **30**, 581–590.

Wei, T., Fife, P., Klewicki, J. & McMurtry, P. 2005 Properties of the mean momentum balance in turbulent boundary layer, pipe and channel flows. *J. Fluid Mech.* **522**, 303–327.

Wosnik, W., Castillo, L. & George, W. K. 2000 A theory for turbulent pipe and channel flows. *J. Fluid Mech.* **421**, 115–145.

Wu, X., Schluter, J., Moin, P., Pitsch, H., Iaccarino G. & Ham, F. 2006 Computational study on the internal layer in a diffuser. *J. Fluid Mech.* **550**, 391–412.

Zagarola, M. V., Perry, A. E. & Smits, A. J. 1997 Log laws or power laws: The scaling in the overlap region. *Phys. Fluids* **9**, 2094–2100.

Zagarola, M. & Smits, A. J. 1998 Mean-flow scaling of turbulent pipe flow. *J. Fluid Mech.* **373**, 33–79.